

ARTICLE TYPE

Analysis of an open foam generated from computerized tomography scans of physical foam samples

Christophe Leblanc*¹ | Nanda Gopala Kilingar¹ | Anne Jung² | Karim Ehab Moustafa Kamel³ | Thierry Jacques Massart³ | Ludovic Noels¹ | Eric Béchet¹

¹Faculty of Applied Sciences - Aerospace & Mechanical Engineering, University of Liège, 4031 Liège, Belgium

²Applied Mechanics - Foams and Metamaterials, Saarland University, 66123 Saarbrücken, Germany

³Architecture & Town Planning Department (BATir), Université Libre de Bruxelles, 1050 Bruxelles, Belgium

Correspondence

*University of Liège, 9 Allée de la Découverte, 4031 Liège, Belgium. Email: christophe.leblanc@uliege.be

Summary

The present article introduces an automated procedure to construct geometrical Representative Volume Elements (RVE) of open-foam cellular materials from computerized tomography (CT) images, with the final aim of generating meshable geometries usable in the Finite Element Method (FEM) used in order to analyse their mechanical behaviour. The methodology consists in growing and fitting a set of ellipsoids to each of the foam cells. These ellipsoids are seeded by local maxima of the distance to the struts obtained from computer tomography images. This methodology is thus fully voxel-based and does not depend on any assumption about statistical distributions of the foam cells. Therefore, it is able to reproduce an accurate geometrical model of the foam's microstructure and its possible irregularities. Moreover, this procedure allows the processing of large 3D data sets that do not fit the random access memory (RAM) by slicing it into smaller independent chunks. The effectiveness of the proposed approach is illustrated by comparing it to FEM simulations for which meshes are obtained from a feature reconstruction approach. Both FEM simulations are then compared with experimental results of uniaxial compressions of an open foam.

KEYWORDS:

Material science, Foam, Tomography, Boundary representation, Finite element methods

1 | INTRODUCTION

Nowadays, cellular materials represent a promising approach for obtaining simultaneously optimised strength, stiffness, dissipation, and weight reduction, and are increasingly used in numerous engineering applications. Among other things, they are used as insulators, filters and crash absorbers^{1,2}. In particular, the class of open-foam materials has found countless applications in many domains such as energy absorbers³, vibration damping⁴, hydrogen production⁵ and aerospace⁶, for instance. As a matter of fact, cellular materials also exist in nature such as in bones or wood.

Manufacturing of metallic foams can be achieved via several processes. One approach for producing open-cell metallic foams is to turn to the technique of electro-deposition onto a sacrificial polymer foam with open-cells. The polymer phase is then etched away, resulting in an open foam with hollow struts⁷. Metallic foams can also be manufactured by direct gas injection into melt, the viscosity of which is controlled by temperature and by adding ceramics powder. This technique is extensively used to obtain

⁰**Abbreviations:** B-REP, boundary representation; CT, computer tomography; FEM, finite element method; RAM, random access memory; RVE, representative volume element. RSA, random sequential addition

aluminium alloy foams. For an extensive survey of metallic foam manufacturing techniques, the interested reader can refer to⁸. Metallic foams manufactured by electro-deposition inherit the morphological characteristics of the underlying polymeric foams. Their microstructure is complex and consists in an interconnected network of ligaments located along the edges of randomly packed cells. In this regards, such metallic foams share structural similarities with equilibrated liquid foams, such as dry soap foam and soap froth, where the cells originated from bubbles separated by tensioned liquid films adopt the shapes of near-polyhedral volumes. Under conditions of mechanical equilibrium where the surface free energy is minimised, these latter foams obey locally Plateau's laws^{9,10}. Under these conditions, each face adopts a constant mean curvature and each face meets at each cell edge at equal dihedral angles of 120° ; while each vertex is adjacent to four edges joining at equal tetrahedral angles of $\cos^{-1}(-1/3) = 109.47^\circ$.

In the current context, there is a need to develop open foams models able to predict the homogenised or apparent behaviour based on the microstructural features. The improvements in computer tomography during the last decade made the direct observation of the foam internal microstructures easier¹¹, and this approach has been used extensively for building geometrical foam models^{12,13,14,15}. Though very detailed, images obtained from computer tomography need to be pre-processed in order to allow their use as a geometrical basis in FEM models. Generally, the pre-processing involves, among other steps, a watershed and (optionally) a H-maxima transform^{12,2,16,17}, both of which can be computationally expensive. Some efforts have been made to assess this difficulty, by either designing new algorithms with improved runtime complexity^{18,19,20}, or by parallelising them^{21,22}. Computing a watershed transform remains nonetheless memory expensive for large 3D images.

One strategy to avoid these computationally expensive steps is to resort to direct image discretisation^{23,14}. However, obtaining FEM models from discretised images^{24,25} remains a daunting task since characterising large data samples requires both time and computational capacity, as well as frequent user input; currently restricting this method to smaller samples²⁶. An interesting strategy, though, has been proposed in²⁷. It consists in coupling extended finite element methods (XFEM) with level sets on non-conforming meshes. The use of non-conforming meshes allows to alleviate near zero or negative Jacobian mesh element issues. Indeed, the complex geometry of the microstructure is implicitly encoded by the level sets. Elements of the non-conforming mesh intersecting the level sets are then locally enriched within the XFEM framework in order to take into account the presence of physical interfaces.

Another possibility is to turn to idealised microstructural geometries. One advantage of this approach is to allow exploring the basic mechanisms linking the microstructure of the considered material to its mechanical behaviour. A simple model using rectangular prisms, as proposed in¹, can already provide some insights. However, a better idealised microstructure has been proposed by Kelvin²⁸ whose model tessellates space with a minimum partitional area using tetrakaidecahedra cells. Kelvin's model has been later improved by the Weaire-Phelan foam model²⁹. As these models show a highly periodic geometry, they are unable to capture the randomness of real microstructures, and, consequently, are poorly effective for capturing the mechanical properties of real foams.

To tackle this randomness issue, various strategies were proposed in the literature (see, e.g.^{30,31,32} to mention a few). A straightforward strategy is to start from a periodic cell structure and add some imperfections to it. This method has been studied in³³, leading to a better agreement with experimental data for the elastic response and the plateau stage. A common strategy consists in using Voronoi tessellations that are based on a distribution of nuclei³⁴; and their generalisations, especially the Laguerre tessellations^{35,2,36}. The Laguerre tessellation is a form of weighted Voronoi tessellation in which the space is partitioned using random packings of spheres of different radii instead of pointwise nuclei. Though versatile and leading to more realistic geometric representations, Laguerre tessellations are not of straightforward use. Indeed, the question arises of how to randomly pack the spheres (loosely or densely), following which distribution (normal, log-normal, gamma, Poisson...) and how to choose the sphere radii. The link between these model parameters and geometric characteristics of foams (such as the porosity, the average pore size and the pore size variation) is also far from being trivial and has been the subject of numerous studies^{37,38,39,40,41,42}. However, Laguerre tessellations are not able, by construction, to capture non-convex cells, cells with curved boundaries, and suffer from the inconsistency of presenting seedless cells⁴³. Also, when available, a Laguerre tessellation does not fully exploit the voxel-informations present in CT-images. These issues have motivated the development of more generalised models exploiting voxel information and/or generalised metrics such as in^{44,45,46,11,47,48,49}, and the present article.

Another approach for trying to generate realistic foam geometries consists in randomly packing spheres. Numerous packing algorithms can be found in the literature and can be classified under collective rearrangement, sequential addition or sedimentation methods⁵⁰. For instance, the random sequential addition consists in adding one by one spheres with randomly chosen diameters under the action of some "gravitational" field. In order to obtain a packing as tight as possible, simulated annealing can be used subsequently in order to randomly perturb the locations of the spheres and improve the tightness of the packing.

Another option is to start with a very dense configuration of large overlapping spheres and then reduce stepwise their diameters and locations in order to reduce the overlapping⁵¹. However, in order to reproduce accurately the morphological parameters of the considered foam, some minimization criterion has to be designed; which is a task far from being trivial. To this aim, strategies using surface minimisation principles by evolving tessellations thanks to the Surface Evolver Software have been studied^{52,53,54}. Moreover, in the case of poly-dispersed spheres, some statistical distribution for the sphere diameters must be chosen (e.g., Poisson, log-normal, gamma or Gaussian)¹⁰. Finally, from these algorithms it is only possible to reconstruct convex cells and tessellation of the obtained packing only provides infinitely thin struts/walls that need to be “dressed”. Despite all these issues and difficulties, random packing algorithm have been extensively used in conjunction with Voronoi tessellations⁵⁵ as well as Laguerre tessellations^{56,57}.

All in all, the above idealised models are able to reproduce accurately foam morphological parameters such as cell-size distribution, face-by-cell count and edge-by-cell count; provided that the considered sample is large enough to be statistically representative of the overall foam⁵⁸. However, they fail to account for local morphological variations as, for instance, struts cross-section shape, variation of cell wall curvatures, local defects (such as damaged or partially missing struts) or the existence of partially reticulated foams (presenting an intermediate state between closed and open microstructures). Such instances of local morphological changes require further construction⁵⁹. In order to introduce these microstructural features, the Distance Neighbour based Random Sequential Addition (DN-RSA) was developed in⁶⁰ and enriched in⁶¹ to represent struts complex morphologies through level set functions.

An alternative model was also developed by^{62,63} in order to overcome some issues and limitations of random packing algorithms. This model consists in generating a “skeletal” foam using a Voronoi tessellation constructed from randomly packed mono-dispersed spheres. The constructed ligaments are then “dressed” with a circular cross-sections the areas of which vary along the length of ligaments; based on empirical expressions developed from in-situ measurements. Nevertheless, though these models are able to produce faithful geometries (at least statistically¹) and quality meshes for FEM simulations, they still requires some input parameters that are difficult to assess.

As geometrical features have a considerable impact on the mechanical behaviour of foams^{64,65}, manufacturing cellular materials with the desired mechanical behaviour is a challenging task. Indeed, on the one hand, foams exhibit a large versatility in their physical characteristics (mechanical, thermic or electromagnetic); allowing a large field of applications. On the other hand, obtaining a specific physical property can be complex and cumbersome as the link between a given property and a foam’s microstructure is far from being trivial. Inside a same sample, different pores may have variable mechanical properties⁶⁶. Moreover, ensuring the production of foams with nominal and stable microstructural and mechanical properties is still a challenging task in the research and industrial domains^{15,8}. As a consequence, there is a significant demand for quality control and characterisation of new foam products in the industry. In this context, reliable computerized foam models that require minimum user input and reasonable computer means are of potential use²⁶. Such numerical model may need to exploit the geometrical information of Representative Volume Elements (RVEs) obtained from computer tomography scans (CT-scans) of foam; while requiring affordable computer resources.

In this work, two reconstruction methods from CT-scan images are developed in order to construct meshable RVEs for finite element simulations. The first model exploits the tool developed in⁶¹ to construct detailed features from distance fields. Contrary to the work⁵⁰ in which the distance field are constructed from a RSA packing, in the present work the distance fields are based on extracted CT-scan images of open foam morphologies, from which the open foam geometries can be reconstructed. This tool will be called *DN-CT-SCAN* in the following.

The second geometric model, referred to in the following as *Ellipsoidal Model*, relies on the Poisson surface reconstruction⁶⁷ from points and normals associated to the exterior surfaces of ellipsoids. It allows obtaining a closed surface representation of the considered foam. The surface provided by the Ellipsoidal Model can subsequently be meshed for based Finite Element Methods (FEM) simulations. Providing a geometric model with the properties of a B-REP instead of a mesh offers the possibility to “tune” to some extent the mesh generated from that B-REP (for instance different levels of mesh refinements can be generated from the same geometric surface). In the present article, the three-dimensional mesh generator used is Gmsh⁶⁸.

Both geometric models rely on the construction of sets of ellipsoids or associated polyhedra. These sets are generated from an original image analysis procedure (described in Section 2.2) which “grows” ellipsoids inside associated polyhedra using the voxel information of CT-scan images, which act as “obstacles” to the ellipsoid growths. Moreover, both memory expensive watershed and H-maxima transform are replaced by clustering and merging of overlapping ellipsoids. For the Ellipsoidal Model,

¹In the sense that the main statistical geometric features of the considered foam, such as the cell-size distribution, the mean number of faces per cell, etc., are reproduced.

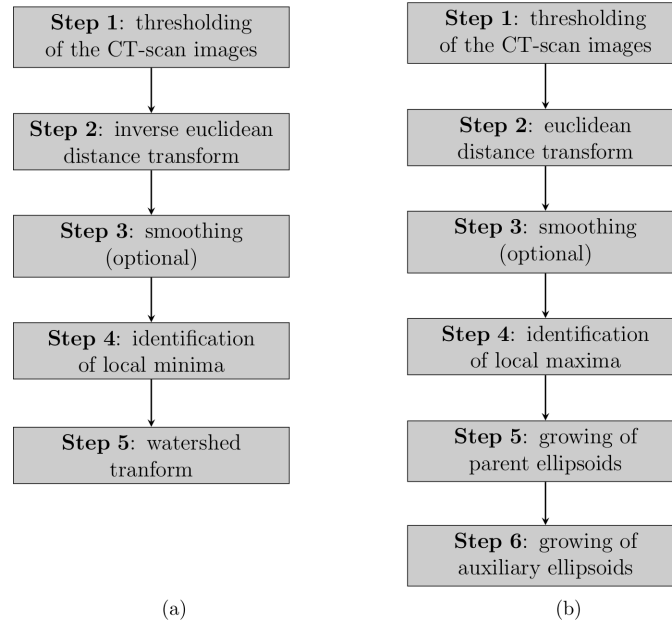


FIGURE 1 (a) Classical image processing steps. (b) Proposed image processing steps.

“auxiliary” ellipsoids are then grown from the surface of their “parent” ellipsoids in order to better fit local features present in the CT-scan. These parent ellipsoids and associated polyhedra are provided to the DN-CT-SCAN model for it to compute its distance fields.

Last but not least, the image analysis procedure has been designed to support the processing of large CT-scan images, i.e. data that cannot be put entirely into the RAM. This feature is achieved by using the Insight Toolkit (ITK) framework⁶⁹ and its streaming capabilities⁷⁰: large CT-scan images can be processed slice-by-slice by loading only one image slice at a time into the RAM. This specific feature allows even standard consumer computers to process large CT-scan images, at a cost of a larger computational time and with a limitation on the maximum allowed cell-size in the CT-scan image. These costs and limitations will be detailed later-on in the present article.

The remainder of this article is organised as follows. Section 2.1 describes how the CT-scan images are processed in the literature, while Section 2.2 describes the proposed image analysis steps, along with the corresponding streaming capabilities (Section 2.3). Section 2.4 explains the advantages of the proposed image analysis in terms of peak memory usage compared to standard image analysis steps, and especially the watershed transform. An image analysis application with the proposed steps is then carried on a cubic aluminium foam sample in Section 3, where two reconstruction models are presented; namely, the DN-CT-SCAN model and the Ellipsoidal Model, which use the ellipsoids and/or the polyhedra obtained from the image analysis steps of an open foam sample. Finally, in Section 4, two FEM simulations, using the generated geometries obtained from both reconstruction models of the open foam case, are carried out under uniaxial compression. Results from FEM simulations associated to both geometric models are then compared with respect to experimental data taken from⁶⁶.

2 | IMAGE ANALYSIS

2.1 | Standard image analysis procedure

The microstructure of a foam sample is described in terms of geometric characteristics of its cells. Identifying these cells and extracting the associated geometric characteristics from grey-level CT-scan images requires the use of a chain of image processing algorithms². The aim of this processing chain is to unequivocally identify the cells and their shapes. A typical processing chain is given in^{16,2} and outlined in Figure 1.

In principle, identifying the cells is easy: it is only necessary to identify where the distance transform (step 2) vanishes to zero and the cell centres are identified as the local minima of the distance transform. However, in practice, the distance transform may present several local minima for a given cell. As a consequence, superfluous local minima have to be removed. Typically,

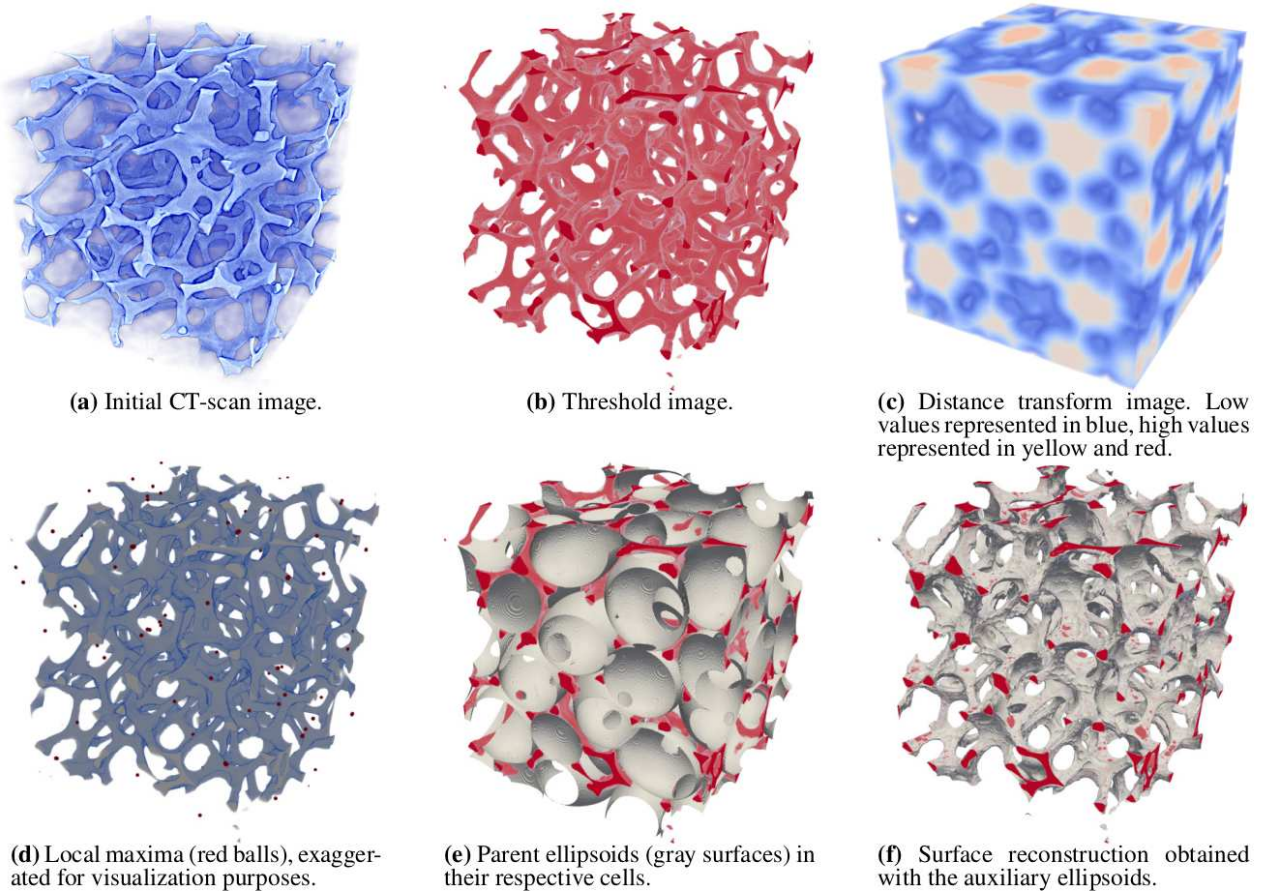


FIGURE 2 Example of the proposed processing steps on a 3D CT-scan image of an open aluminium foam. Subset of the $613 \times 598 \times 621$ described in Section 3.1.

this is achieved using morphological transforms such as a watershed transform, optionally preceded by a (possibly adaptive) H-maxima transform^{2,71,72,12} or even a grey-scale reconstruction¹⁸, in order to avoid cell “oversegmentation”.

2.2 | Proposed image analysis procedure

The standard image analysis steps usually require the use of morphological algorithms, such as the watershed transform, for unequivocally identifying cells. These algorithms are computationally heavy, despite efforts for tackling the issue (see e.g. ^{18,21,20,22} for the watershed transform). The present contribution presents an alternative processing chain for identifying cells as outlined in Figure 1.

This alternative processing chain replaces the watershed transform (and, optionally, the H-maxima transform or other smoothing algorithms) by a stage of growing and clustering ellipsoids. This, as it will be shown later, is memory-wise much cheaper than morphological algorithms since it does not operate at the voxel level, as the investigation conducted in Section 2.4 on some artificially generated foams samples and a real-world foam indicates.

This processing chain has been implemented using the ITK library as backbone⁶⁹. The ITK library is handful and versatile: it allows the user to construct its own processing chain using a large choice of pre-implemented algorithms, as well as implementing customised algorithms which can be integrated in any processing chain. The capabilities of the ITK library can be handful if some CT-scan images need extra processing steps due to some particular characteristics. The different proposed processing steps are described hereafter.

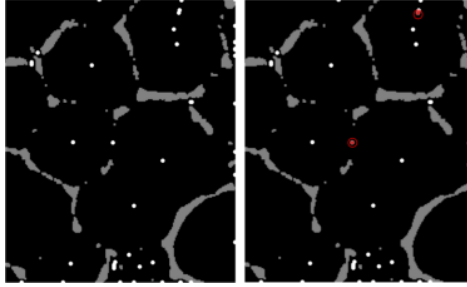


FIGURE 3 Discarding some local maxima based on the eigenvalues of their associated local Hessian. White enhanced points: local maxima. Grey: cell walls. Red circled maxima: saddle points to be discarded (2D case).

2.2.1 | Step 1 - Threshold

The threshold of grey-level images is obtained by the simple histogram-driven algorithm of Ridler and Calvard^{73,74}. The results is a black and white binary 3D image. Naturally, following the needs, any other threshold algorithm may be used here. A threshold example is given in Figure 2-b.

2.2.2 | Step 2 - Distance transform

The euclidean distance transform is computed by means of the algorithm of Maurer⁷⁵. Applied on a black and white image (as illustrated in Figure 2-c), where, for instance, white voxels represent cell struts/walls, this transform replaces the intensity values of the black voxels by their euclidean distance to their respective closest white voxels. White voxels have their intensities values set to zero.

2.2.3 | Step 3 - Distance post-processing

This step is optional, if some post-processing of the distance transform is needed, it can be added here. For instance, a smoothing step may be desirable for avoiding superfluous local maxima and oversegmentation¹⁶. For the data sets used in this article, such optional processing step was not proven necessary and none was used.

2.2.4 | Step 4 - Local maxima

The identification of local maxima is performed thanks to a customised three-dimensional implementation of the algorithm of Pham⁷⁶. The algorithm provided by ITK for locating local maxima was not used here because it is not provided with streaming capabilities. On the contrary, the algorithm of Pham⁷⁶ consists in collecting local maxima candidates by scanning voxels along lines. The local maxima candidates are then compared against a constant neighbouring of voxels Nr . These characteristics make this algorithm easy to adapt for streaming.

Local maxima are then selected following the eigenvalues or their associated local Hessian, computed from the distance transform. Computing the local Hessians, and thus the local second derivatives, in a discrete image is an ill-posed problem. In order to compute the local second derivatives as accurately as possible, the ITK filter “HessianRecursiveGaussianImageFilter” was used. This filter uses a discrete convolution with a Gaussian kernel of standard deviation σ on the considered image prior to computing the derivatives. More details about how the local Hessians are computed can be found in⁷⁷. Local maxima with associated negative Hessian eigenvalues ($\lambda_i < 0$) or with all negative Hessian eigenvalues except one which is such that $|\max_i \lambda_i| \leq \epsilon |\min_i \lambda_i|$ (with the Hessian threshold ϵ being a small value) are selected. Other local maxima are discarded as they actually correspond to saddle points. This selection procedure does not aim at discarding all superfluous maxima. Instead, its objective is to avoid having them located between two cells; as it may occur for open foams. Figure 3 shows a 2D example were some local maxima are discarded. Figure 2-d gives an example applied to a 3D CT-scan data set.

2.2.5 | Step 5 - Parent ellipsoids

Obviously, even if some superfluous local maxima are discarded on the basis of the eigenvalues of their associated Hessian, most of them are still present at this stage. From the local maxima, even superfluous ones, ellipsoids are associated as follows.

The ellipsoids are initially set as unit spheres centred at the local maxima positions. They are then grown by an optimisation procedure described in⁷⁸. This optimisation procedure iteratively grows ellipsoids inside associated polyhedra. At each iterations the associated polyhedra are constructed from their current respective ellipsoids and the surrounding obstacles (here, the voxels corresponding to struts in the considered CT image). Once the polyhedra are constructed, the ellipsoids are grown by one more increment. This process is repeated until the relative volume variation of each ellipsoid drops below a prescribed threshold.

Ellipsoids are indeed able to capture cell anisotropies, which is considered as a necessity for assessing the mechanical behaviour of foams^{1,79,80,81}. Although sets of growing spheres are able to capture some foam anisotropies⁸², it is believed that ellipsoids lead to better results by capturing more precisely local cell features^{83,47,48}.

It should be noted that the idea of modelling the geometry of a foam as the result of a growth process, as presented above, is not new. The Voronoi and Laguerre tessellations can be defined as the result of a growth process of spheres⁵⁶. For growth of spheres, the idea has been explicitly exploited in, e.g.⁸². Growth of ellipsoids in the context of polycrystalline microstructures reconstruction has been proposed in⁸³. More recently, algorithms implementing ellipsoid growths for fitting cell have been presented by A. Alpers et al.⁴⁶ and improved by O. Sedivy et al.^{47,48}. These algorithms try to optimise an objective function encoding the positions and shape factors of all ellipsoids. The objective function tries to maximise ellipsoids volumes while avoiding voxels representing boundaries between crystal grains. Obviously, the optimisation problem becomes rapidly high-dimensional as the number of parameters to consider grows linearly with the number of ellipsoids. This issue has been tackled in⁴⁸ with an heuristic approach. In this approach, only a subset of parameters are optimised at each step, using simulated annealing. Though faster, the algorithm proposed in⁴⁸ still requires on the order of several million of iterations to converge. On the contrary, the algorithm proposed by R. Deits et al.⁷⁸ maximises the volumes of the considered ellipsoids independently. As a consequence it breaks down the high-dimensional optimisation of E. Alpers in a set of independent low-dimensional optimisation problems. Indeed, since each ellipsoid volume is independently maximised, only nine parameters (three for the position of the centre and six for the shape factors) need to be optimised. Therefore, the number of ellipsoids (and thus cells) that can be optimised is much higher than with the approaches of E. Alpers and O. Sedivy. Moreover, the algorithm presented by R. Deits can be trivially parallelised. A drawback, though, of the approach of R. Deits et al. is that there is no guarantee that ellipsoids are not overlapping. However, this drawback is not a concern for us as subsequent steps do not depend on this peculiarity. Therefore, the approach proposed by R. Deits for growing ellipsoids has been chosen as it can process a large number of ellipsoids while being less computationally expensive than the approach suggested by O. Sedivy.

Once superfluous ellipsoids (associated to superfluous local maxima located in the same cell) have been grown, they are clustered together by using the *Generalized Density-Based Scan* (GDBScan) algorithm⁸⁴. Since ellipsoids that have been grown in the same cell (even from different starting local maxima) are more likely to overlap than ellipsoids grown in two different cells, the criterion for associating two ellipsoids in the same cluster is based on their relative intersecting volume. More precisely, two ellipsoids \mathcal{E}_1 and \mathcal{E}_2 potentially associated to the same cell, are clustered together if their associated volumes satisfy one of the relations (1).

$$\frac{Vol(\mathcal{E}_1 \cap \mathcal{E}_2)}{Vol(\mathcal{E}_1)} \geq \tau \quad \text{or} \quad \frac{Vol(\mathcal{E}_1 \cap \mathcal{E}_2)}{Vol(\mathcal{E}_2)} \geq \tau \quad (1)$$

Where $\tau \in [0, 1]$ is the relative intersection volume threshold. When τ is set close to zero, any slightly intersecting pair of ellipsoids will be clustered together; while for τ set close to one, only pairs of almost overlapping ellipsoids will be clustered together. In general, a suitable guess value for this parameters will be $\tau \approx 0.5$.

Finally, ellipsoids identified by the above criterion as belonging to a same cluster are merged together into one ellipsoid using the *Minimum Volume Covering Ellipsoid of Ellipsoids* (MVCEE) algorithm detailed in⁸⁵. Figure 2-e shows an example of computed parent ellipsoids.

2.2.6 | Step 6 - Auxiliary ellipsoids

“Auxiliary” ellipsoids are grown using the previously expanded ellipsoids for generating new seeds. These “auxiliary” ellipsoids are constructed as follows (see Figure 4): each previously grew ellipsoid is uniformly discretised into a set of points and serves as “parent” to its associated auxiliary ellipsoids. This discretisation is parametrised by an azimuthal angle increment $\Delta\theta$, which drives, in turn, the polar angle increment

$$\Delta\phi_i = \frac{2\pi}{\lfloor 2\pi \sin(\theta_i)/\theta_i \rfloor + 1} \quad (2)$$

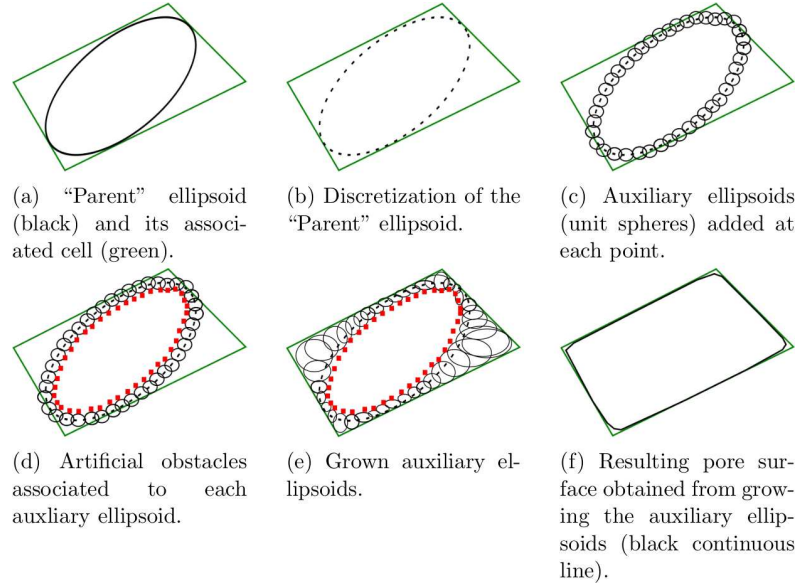


FIGURE 4 Schematic sequence illustrating the growth of auxiliary ellipsoids into a cell. The last step f. is obtained by taking the zero iso-surface (iso-line) of the distance field to the ellipsoids.

Where $\theta_i = \theta_{i-1} + \Delta\theta$ is the i th increment in angle θ , and $\lfloor \cdot \rfloor$ returns the closest lower integer of its argument. Once the discretisation computed, each of the associated point is attached to an auxiliary ellipsoid. Initially, these auxiliary ellipsoids are simply spheres the radii of which are one voxel wide. Then, between each sphere and the centre of the "parent" ellipsoids an "artificial" obstacle is added. These obstacles are simply the closest points of each sphere to the centre of the parent ellipsoid. The aim of these "artificial" obstacles is to avoid the auxiliary ellipsoids to all decay into their parent ellipsoids. Once initialised by unit spheres and their associated artificial obstacles, the auxiliary ellipsoids are then grown using the same algorithm as their parent ellipsoids⁷⁸, taking into account for each auxiliary ellipsoid the same obstacles as for its associated parent ellipsoid and the artificial ones generated from it and the spheres. The result shown in Figure 4-f is obtained by extracting the zero iso-surface of the distance field to the ellipsoids.

From all the above described steps, an approximation of a CT-scan image of foam in terms of a set of ellipsoids (and associated polyhedra) can be obtained. This set can then be used to reconstruct the geometry of the foam as demonstrated in Section 3; geometry that can be subsequently used into a FEM simulation (see Section 4). These steps avoid the memory expensive watershed and H-maxima transforms, replacing them by the clustering and merging of overlapping ellipsoids. Depending on the number of auxiliary ellipsoids associated to each "parent" ellipsoid, the obtained set of ellipsoids allows a rather precise fitting of the struts structure present in the CT-scan images, including local defects such as partially missing or deformed struts.

2.3 | Proposed image analysis procedure with streaming

Streaming is the ability to process an image by slices. It offers the advantage to be able to process large amounts of data that are not manageable otherwise (e.g. that do not fit the RAM of a computer, and/or parallelise the processing). The Insight Toolkit framework⁶⁹ offers such streaming capabilities⁷⁰. All the steps described in Section 2.2 have been implemented as ITK filters which are streamable along slices (Figure 5).

2.3.1 | Streaming of threshold (step 1)

The streaming of the threshold in the proposed image analysis does not pose difficulties. Since threshold algorithms mostly operate voxel by voxel, they are streamable without any modification.

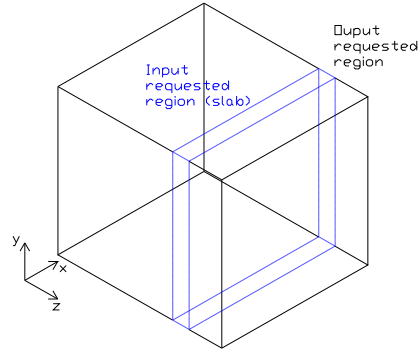


FIGURE 5 Extraction of a slice from a 3D image.

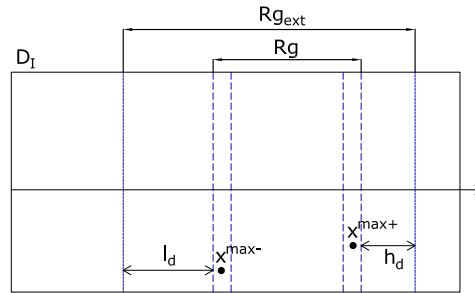


FIGURE 6 Computation of the correct distance transform on slice Rg , by computing an incorrect distance transform on slice Rg_{ext} . See text for details.

2.3.2 | Streaming of distance transform (step 2)

The streaming of the distance transform is less straightforward: computing the distance transform only on one slice will generally provide an incorrect transform on that slice. This is due to the fact that some voxels outside the considered slice may influence the computation of the distance inside that slice. It is nevertheless possible to overcome this difficulty by computing an incorrect distance transform on a thicker slice Rg_{ext} so as to ensure a correct distance transform inside the initial slice Rg . The thicker slice Rg_{ext} is computed as follows (see Figure 6): first, an incorrect distance transform is computed on the initial slice Rg . Second, voxels x^{max-} and x^{max+} on the boundaries of Rg with maximum associated (incorrect) distances l_d and h_d are searched for. Third, the slice Rg is extended to Rg_{ext} along both directions by, respectively, l_d and h_d voxels. Finally, an incorrect distance transform is computed on Rg_{ext} , with the guarantee to be correct on slice Rg .

2.3.3 | Streaming of distance post-processing (step 3)

If some additional filters are added in **step 3**, the user must ensure that they are streamable in order to benefit from this feature.

2.3.4 | Streaming of local maxima (step 4)

The computation of local maxima from the distance transform in section 2.2.4 requires modifications to the original algorithm of Pham⁷⁶: it needs to “scan” along voxel lines for local maxima candidates. The algorithm has been implemented such that these voxel lines are always located inside a given slice. Computation of local maxima candidates by this algorithm is thus exact. Local maxima are then selected from candidates by analysing the values associated to their neighbouring voxels in a region of radius Nr . In order to ensure a correct computation of the local maxima inside the current slice Rg , the same procedure as described earlier for step 2 is used: the current slice Rg is extended to a thicker slice Rg_{ext} where the (incorrect) maxima are looked for, and the (guaranteed correct) maxima inside slice Rg are returned. The computation of the thicker slice Rg_{ext} is, however, simpler than in step 2: extension distances l_d and h_d are simply equal to the radius of the neighbouring search region Nr .

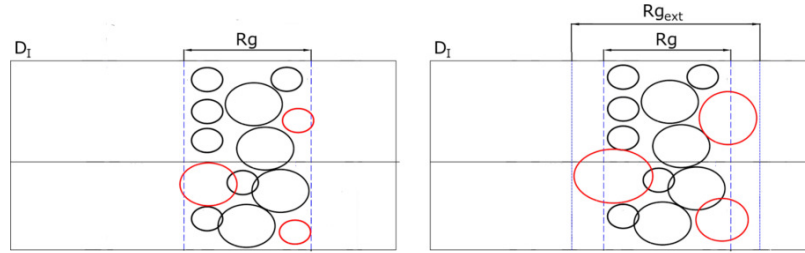


FIGURE 7 Growth of ellipsoids inside a slice R_g . If some ellipsoids grew outside R_g (red ellipsoids), their growths are recomputed in a thicker slice $R_{g_{ext}}$ until no more ellipsoids grow outside the last considered slice.

2.3.5 | Streaming of ellipsoid growth (steps 5 and 6)

Regarding the growing of parent and auxiliary ellipsoids (Sections 2.2.5 and 2.2.6), a similar strategy as in Sections 2.3.2 and 2.3.4 is used. Ellipsoids with centres located inside the current slice R_g are grown. If some of the ellipsoids grew outside of the current slice R_g , their growths are recomputed within a thicker slice $R_{g_{ext}}$ (see Figure 7). If the slice $R_{g_{ext}}$ is not thick enough (meaning that there are still some ellipsoids which grew outside this slice) then, the slice $R_{g_{ext}}$ is extended further until no more ellipsoid grows outside it or if a boundary of the CT-scan images is reached (meaning that there are no more voxel data available beyond the extended region $R_{g_{ext}}$).

2.3.6 | Discussion

With the adaptations described above, it is possible to use the proposed image analysis procedure within a streaming framework, provided that each optional added filter (step 3) is also streamable. As shown in Section 2.4 this allows processing CT-scan data of foams that would normally not fit in the available RAM. Nonetheless, there is one downside and one limitation when using streaming. The downside is that the computational time for processing the whole considered image will increase compared to a normal image analysis procedure (where the whole CT-scan data is fitted into the RAM). This is caused by the fact that some algorithms used for the image analysis procedure have to be called twice. That fact can be seen as “communication costs” between slices. The scalability is thus not one as expected with any parallelised setting. Regarding the limitation, there is no strict guarantee that the extended regions $R_{g_{ext}}$ will not cover the entire CT-scan data set (and thus obliterating the whole point of doing streaming). As a matter of fact, the biggest extended region $R_{g_{ext}}$ will approximatively be of the size of the biggest cell present in the foam. In general, cells seldom span an entire foam sample, especially for large samples. Thus, the memory benefits obtained by streaming can be significant.

2.4 | Memory usage

Memory usage can be considered as an issue regarding the techniques of geometric reconstructions of foams. Indeed, storing in the RAM the CT-scan data alone may already be an impossible task for standard computers (such as consumer market computers), even less regarding the processing of those data. The above proposed image analysis procedure aims to overcome this limitation by trying to use less RAM than a standard image analysis procedure (and, especially, the watershed). Moreover, its streaming ability offers the possibility for standard computers to process CT-scan data that would not even fit their RAM.

In order to determine the ability of the proposed image analysis procedure, an investigation has been conducted on an artificially generated honeycomb foams of different sizes. For the sake of comparison, every foam has the same cell size. An example of such artificially generated foam can be seen on the left of Figure 8.

Table 1 reports the sizes of the different generated artificial honeycomb foams along with their corresponding number of cells. The cell sizes are kept constant for all honeycomb foams. Table 1 also reports the theoretical minimum amount of RAM needed for storing the corresponding data, assuming 8 bytes per voxel. The last three columns display the measured peak memory usages² for the watershed algorithm (as implemented in the ITK library⁶⁹) and the proposed image analysis procedure without and with using the streaming ability (using 10 slices). The “> 64.0” entry in the table corresponds to a peak memory usage

²Peak memory usages were measured using the software *valgrind*⁸⁶.

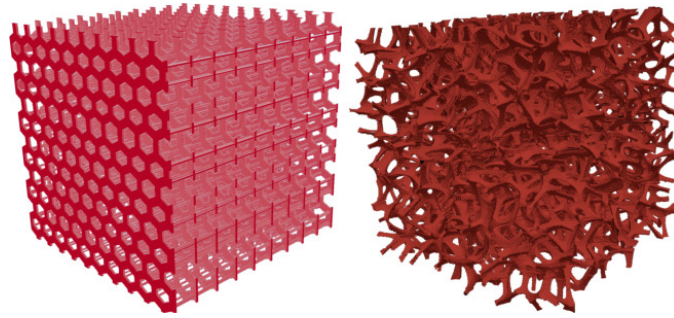


FIGURE 8 Left: artificially generated honeycomb foam of size $600 \times 600 \times 600$ voxels and containing 1430 cells. Right: artificial foam generated using the DN-CT-SCAN model⁶¹ with 616 random inclusions.

exceeding the maximum of 32 GB RAM available (extended to 64 GB RAM thanks to the RAM compression utility *ZRAM*³) of the computer on which this investigation was conducted. It was, therefore, not possible to measure the peak memory usage for this entry of the table.

From Table 1 it can be seen that the proposed image analysis procedure is indeed less memory demanding than the watershed algorithm (as implemented in the ITK library⁶⁹) for the considered artificial honeycomb data sets. Especially, the usage of streaming allowed reducing the peak memory usage by a large amount. Thanks to streaming, it was possible to process an artificially generated foam of $1800 \times 1800 \times 1800 \approx 5.8 \cdot 10^9$ voxels; which, due to RAM limitations, was possible neither using the watershed nor using the proposed image analysis procedure without using the RAM compression utility *ZRAM*.

It should be noted that, technically, only one bit per voxel is required for storing a thresholded image such as the ones shown in figure 8. However, some filters, such as the (inverse) euclidean distance transform, require at least 4 bytes per voxel in order to perform their calculations. Distance calculations indeed require a floating type, or at least a sufficiently “big” integer type (such as “int” encoded on 32 bits) if one wishes to compute squared distances. Thus, the real storage cost of voxel data is not 1 bit, but at least 4 bytes per voxel. Here, Table 1 considers a worst case scenario were a filter might require 8 bytes per voxel.

Figure 9 displays the peak memory usages for the watershed and the proposed image analysis procedure, with and without streaming (points). It can be noted that, for the generated artificial honeycomb foam, the proposed image analysis has always a lower peak memory usage than the watershed, and that the streaming increases this trend. Roughly, by using ten slices, the streaming was able to use ten times less memory than the watershed. This ability can be an advantage when it comes to process large data sets with limited capabilities, or can authorise the processing of bigger data sets which were not processable earlier.

Diamonds in Figure 9 show the peak memory usages measured for the real-world foam data set that is presented in Section 3.1. Circles show, for their part, the peak memory usages on artificial foams generated using the DN-CT-SCAN model⁶¹, described in section 3.1.3, with random inclusions following a statistical distribution similar to that of the cells of the real-world foam (right of Figure 8). It can be seen that the trends are the same as for the artificially generated foam, indicating that the streaming strategy is likely also effective on real-world foam data.

It should be noted, though, that the earlier mentioned limitation of the streaming capability of the proposed image analysis with respect to the maximum cell size drives the peak memory usage. For instance, if a cell extends across the entire foam sample, the proposed streaming capability will be of no use for reducing the peak memory usage. However, for the purpose of reconstructing foam geometries, the cases of cells extending across the whole foam sample can be considered quite exceptional. Especially, this case should arise less frequently with larger foam samples, for which the usage of streaming can be useful.

³https://kernelnewbies.org/Linux_3.14

TABLE 1 Sizes in pixels, number of cells and minimum RAM (assuming 8 bytes per voxel) needed for storing data for artificially generated honeycomb 3D foams images. Last three columns: measured peak memory usages for watershed and the proposed image analysis procedure with and without streaming

Cube side (voxels)	Nb. of cells	Min. RAM (GB)	Watershed (GB)	Proposed (GB)	Proposed, streaming (GB)
150	120	0.03	0.1	0.05	0.07
300	390	0.2	0.7	0.27	0.17
600	1430	1.6	5.7	2.2	0.8
800	3094	3.8	13.4	5.3	2.0
1200	10,500	12.9	45.1	16.4	4.3
1800	34,410	43.5	> 64.0	59.9	14.9

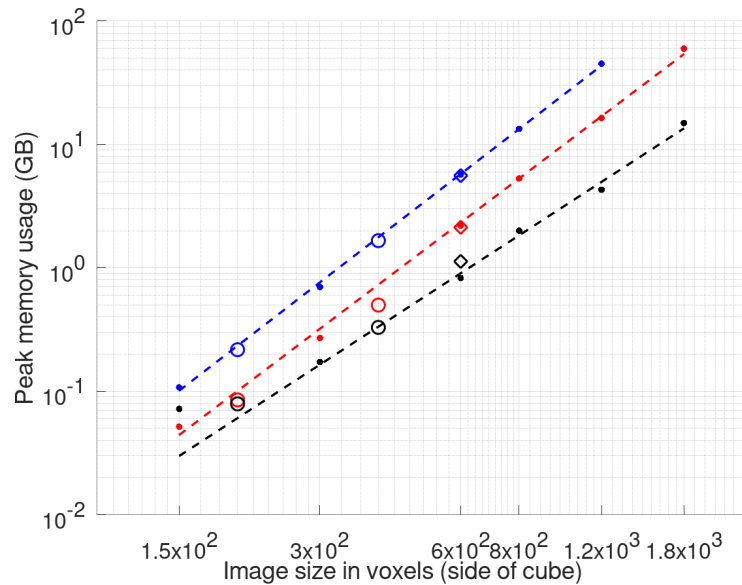


FIGURE 9 Peak memory usages in GB on a set of artificially generated honeycomb foams with constant cell size. In blue: watershed (as implemented in the ITK library⁶⁹). In red and black: proposed image analysis with and without streaming, respectively. Discontinuous lines show the global trends for each method. Diamonds show the peak memory usages for each method on the real-world data set presented in Section 3.1. Circles show the peak memory usages on artificial foam data sets generated by random inclusions using the DN-CT-SCAN model⁶¹ described in section 3.1.3.

3 | APPLICATION TO FOAM RECONSTRUCTION

3.1 | Open foam

3.1.1 | Data acquisition

A cubic aluminium foam ($AlSi_7Mg_{0.3}$) with an edge length of $15 \times 15 \times 15 \text{ mm}^3$ and a pore size of 20 pores per inch (ppi) was purchased from *Celltec Material GmbH*, Dresden, Germany. X-ray computed tomography – performed at the Fraunhofer Institute for Non-destructive Testing (IZFP), Saarbrücken, Germany – was used to determine the real microstructure of the foam. The scans were performed with a resolution of 1984×1984 pixels per layer and a voxel size of $12 \mu\text{m}$. From the raw scanned images, a set of 673 2D-images with a resolution of 711×711 pixels each has been extracted (Figure 10).

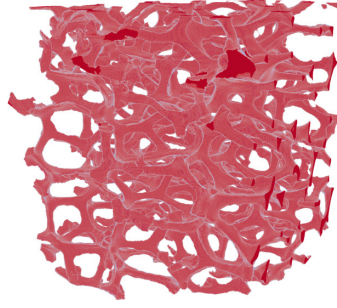


FIGURE 10 3D-image extracted from raw CT-scans of a cubic aluminium foam.

TABLE 2 Parameters used in the image analysis of the CT-scan data presented in Section 3.1.

Parameter	Value	Description
Nr	10	Radius of the neighbouring region for testing local maxima candidates.
ϵ	10^{-5}	Hessian threshold for selecting local maxima.
σ	1.5	Gaussian standard deviation used for the convolution kernel.
τ	0.45	Relative intersection volume threshold.
$\Delta\theta$	10°	Azimuthal angle increment for discretising ellipsoids.

3.1.2 | Image analysis step

The above set of described images contains void boundary regions with no struts at all. Therefore a subsample made of $613 \times 598 \times 621$ voxels was extracted in order to keep only the relevant data. From this subsample, ellipsoids were generated with the procedure presented in Section 2.2. Table 2 gives the parameters that were used. In this subsample each voxel is of length $\approx 24 \mu\text{m}$ in all the directions. Figure 11 shows the ellipsoids obtained in a sub-region cropped, for visualisation purposes, between the 127th and the 484th voxels in each direction. From the images, it can be noticed that one cell corresponds unequivocally to one ellipsoid. Quantitatively, if feature voxels represent the struts (in red in the images), 69% of the non-feature voxels (respectively only 0.3% of the feature voxels) are located inside the ellipsoids; indicating that the ellipsoids indeed fit the cells and do not cross the struts. Figure 12 shows the surfaces obtained from the polyhedra associated to the parent ellipsoids.

Growing auxiliary ellipsoids allows obtaining a much better fit of the cells as shown in Figure 13. Indeed, 96% of the non-feature voxels are now located inside at least one ellipsoid, while still only 0.3% of the feature voxels are located inside an ellipsoid. However, this better fit comes at the expense of optimising a much larger number of ellipsoids (the number of auxiliary ellipsoids grows linearly with the number of parent ellipsoids). Nevertheless, this is not an issue for the algorithm of R. Deits et al.⁷⁸ as only the number of associated optimisation problems will grow and not their dimensions.

In what follows two different geometrical models are used for reconstructing the geometry of a foam and are compared against the experimental image data. Both of these models use, as starting point, the ellipsoids and/or their associated polyhedra obtained from the proposed image analysis procedure given in Section 2.2.

3.1.3 | Reconstruction using the DN-CT-SCAN model

In⁶¹, the authors have developed a method to extract open foam morphologies from inclusions packings using distance functions as described in⁶⁰. In this first model, the reconstruction of the geometry uses the set of ellipsoids that have been generated previously. The ellipsoids can then be used as the initial packing to extract distance functions that can then be treated to obtain open foam RVEs. This method presents the advantage of using experimental information to improve the fidelity.

As described in⁶⁰, nearest neighbour distance functions, $DN_k(\mathbf{x})$ in a point \mathbf{x} , are defined as the distance from the considered point to the k -th nearest inclusion. Figure 14 illustrates some nearest neighbour distance functions on a spherical packing. This

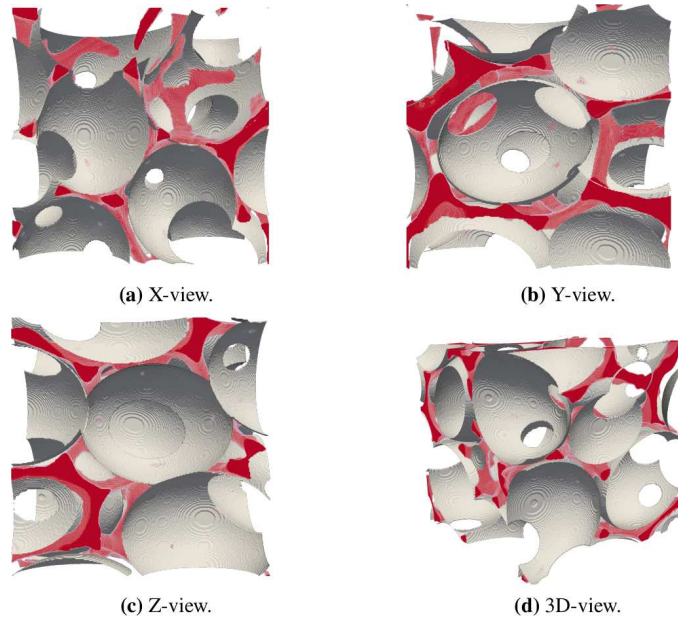


FIGURE 11 Surfaces of the parent ellipsoids (grey) obtained by the proposed image analysis steps and “struts” voxels extracted from the raw CT-scans showed for visual comparison (red). Cropped views of the $613 \times 598 \times 621$ set for visualisation purposes.

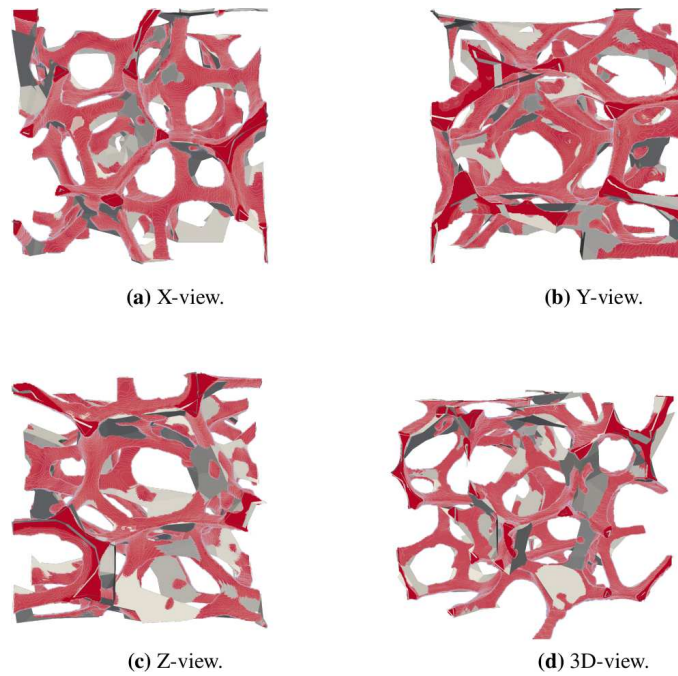


FIGURE 12 Surfaces of the polyhedra (grey) obtained by the proposed image analysis steps and “struts” voxels extracted from the raw CT-scans showed for visual comparison (red). Cropped views of the $613 \times 598 \times 621$ set for visualisation purposes.

step ensures that the distance functions are not affected by the boundary inclusions. The distance functions are then used to extract the modified “Plateau” function,

$$O_P(\mathbf{x}) = \frac{(DN_3(\mathbf{x}) + DN_2(\mathbf{x}))}{2} - DN_1(\mathbf{x}) \quad (3)$$

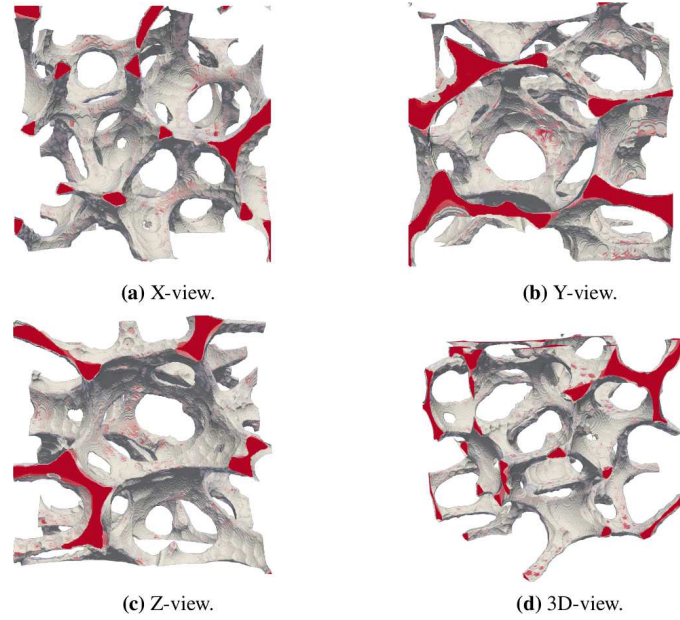


FIGURE 13 Surfaces of the auxiliary ellipsoids (grey) obtained by the proposed image analysis steps and “struts” voxels extracted from the raw CT-scans showed for visual comparison (red). Cropped views of the $613 \times 598 \times 621$ set for visualisation purposes.

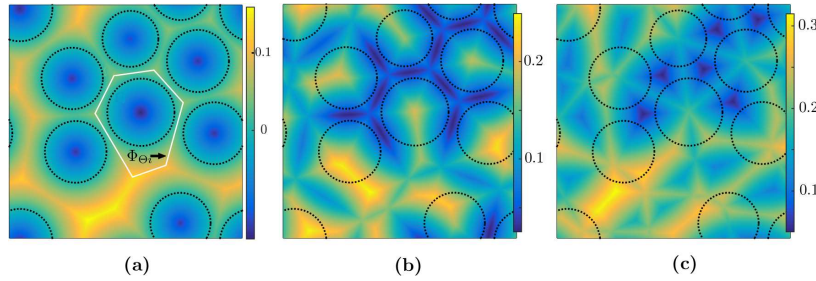


FIGURE 14 Functions (a) DN_1 , (b) DN_2 , and (c) DN_3 .

as described in⁶¹, where $DN_1(\mathbf{x})$, $DN_2(\mathbf{x})$ and $DN_3(\mathbf{x})$ are the 1st, 2nd and 3rd neighbour distance functions respectively. The “Plateau” function enables the extraction of the 3-sided struts.

The evaluation of the nearest distance field did not bring particular difficulty when starting from a sphere packing as in⁶¹. However, in the present case, it is possible that the ellipsoids used as reference and their associated polyhedra intersect. In that case, this distance field DN_k is not monotonically evolving in the intersection region. This problem can be avoided by introducing an offset to the ellipsoid surface. In⁸⁷, the authors have built *Ad-hoc* level set functions using previously computed distance fields. Similar *Ad-hoc* level set functions can be built around the ellipsoids that can then be manipulated to remove residual interpenetrations by introducing a gap between two selected ellipsoid based inclusions (see Figure 15).

The distance field associated to an inclusion i , denoted as DS_i , is defined as the signed distance field which is negative inside the inclusion and positive outside. The distance fields, DS_i and DS_j , resulting from two inclusions i and j , can be used to determine their mutual intersection volume as

$$\max(DS_i(\mathbf{x}), DS_j(\mathbf{x})) < 0, \quad \forall i \neq j. \quad (4)$$

The minimum distance to every inclusion other than inclusion i , $DO_i(\mathbf{x})$, is given by

$$DO_i(\mathbf{x}) = \min(DS_j(\mathbf{x}) : \forall i \neq j), \quad (5)$$

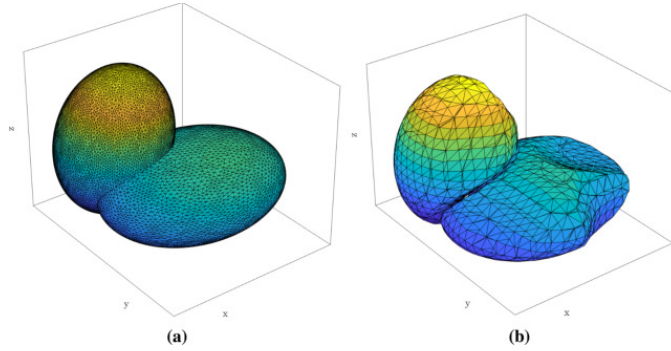


FIGURE 15 (a) Ellipsoids obtained by processing the CT-scan; (b) Post-processing of ellipsoids to avoid residual interpenetration using the method described in⁸⁷.

and an *ad-hoc* level set function, $O_i(\mathbf{x})$, can be then extracted as follows

$$O_i(\mathbf{x}) = \max(DS_i(\mathbf{x}), (DS_i(\mathbf{x}) - DO_i(\mathbf{x}))). \quad (6)$$

The necessary gap can be introduced as an offset, c , such that

$$O_i^g(\mathbf{x}) = \max(DS_i(\mathbf{x}), (DS_i(\mathbf{x}) - DO_i(\mathbf{x}) + c), \quad (7)$$

with the zero level of O_i^g resulting in the necessary inclusion surface of the inclusion i .

The ellipsoids can also be replaced by the polyhedra as the basis inclusion considering that the polyhedra are closer to the foam geometry. Indeed, as described in⁷⁸, polyhedra are defined by the interior region delimited by oriented planes. These planes are determined via the boundaries of the struts and tangents to the surfaces of the associated ellipsoids. Given that the polyhedra always contain their associated ellipsoid but not any strut, they are closer to the foam geometry than ellipsoids. The distance fields for the polyhedra can be similarly generated as for the ellipsoids.

The ellipsoids and polyhedra obtained from the CT-scan in Section 2.2 have the problem of boundary effect due to insufficient information at the boundaries to extract statistically representative inclusions. In order to analyse RVEs that are similar in size to those that were tested experimentally, it is possible to continue the process of adding inclusions using random sequential addition (RSA), as described in⁸⁸. The distance fields obtained previously ensure that the new spherical inclusions are statistically valid to extract open foam morphologies⁶¹. Once the RSA process is complete, an open foam morphology can be extracted using the computed distance fields.

For both packings (ellipsoids and polyhedra), the obtained porosity is around 93.5% which is very similar to that of the original foam of 93%. Thus, the relative densities of the two samples are considered close enough. The obtained RVE mesh was refined as explained in⁸⁸ and a tetrahedral mesh was extracted using the Tetgen software⁸⁹. Figure 16 shows the Hausdorff distances, computed using the software Meshlab⁹⁰ with 500.000 sample points, between the extracted RVEs and the thresholded CT-scan image for both ellipsoid and polyhedral packing. It can be seen, that the polyhedral packing leads to a better representation for the DN-CT-SCAN model. The Hausdorff distance between the reconstructed geometry and the struts is 1.48 mm (corresponding to a relative maximum error of 9.9 %) when using the ellipsoid packing, while it reduces to 0.89 mm (corresponding to a relative maximum error of 5.9 %) with the polyhedral packing. For the polyhedral packing, it can be seen that for a statistically validated representation of the actual foam, the extracted RVE is very close in the reproduction of the various morphological features.

3.1.4 | Reconstruction using the Ellipsoidal Model

In this second model, the reconstruction of the geometry uses the set of parent and auxiliary ellipsoids that have been generated previously in Section 2.2. The procedure for reconstructing the geometry from the set of ellipsoids is conceptually simple. First, all ellipsoids (parent and auxiliary) are discretised to a set of points and associated normals. Then this set of points and normals is used for generating a closed triangulated surface using a Poisson surface reconstruction. Finally, this triangulated surface is meshed using the GMSH software⁶⁸. What follows describes the process in details.

First the iso-surfaces of the parent and auxiliary ellipsoids are discretised into a set of points and associated normals using the same discretisation technique as in step 6 of Section 2.2. The angle increment $\Delta\theta$ is described in Section 2.2 and depicted in

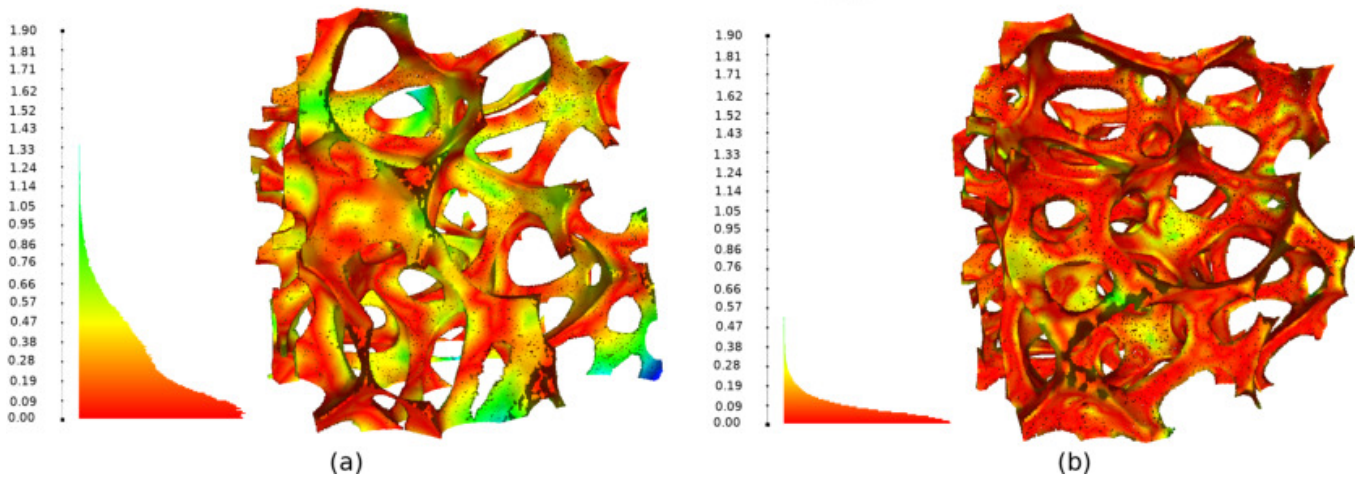


FIGURE 16 Visual representation of the Hausdorff distance in mm between the CT-scan image and the meshes extracted using DN-CT-SCAN. (a) Use of ellipsoidal packing. (b) Use of polyhedral packing.

Figures 17-a and-b. Using this technique ensures that the set of points is approximately homogeneous. Moreover, the ellipsoid's iso-surfaces ISO_{param} on which the points lie can be chosen so that the porosity of the final reconstructed geometry matches as much as possible the measured porosity of the foam. One may notice that the auxiliary ellipsoids already closely fit the real foam geometry. As a consequence, this parameter usually does not need to be fine tuned and can generally be kept at its default value $ISO_{param} = 1.0$; which corresponds to the ellipsoid's surfaces. Then, points associated to a given ellipsoid E_i , but located strictly inside a different ellipsoid E_j (w.r.t. the considered iso-surface) are discarded. This ensures only surface points and associated normals are kept, even if the ellipsoids are intersecting (Figure 17-c).

However, at the boundaries there is insufficient information to extract statistically representative ellipsoids. In order to avoid spurious reconstruction effects a subset of suitable surface points is determined from the set of surface points as follows. First, clipping planes are applied in order to discard points too close to the boundaries (Figure 17-d). Second, "holes" created by the clipping planes in the set of points are filled by adding new points with a similar density as the density of the whole set of surface points (Figures 17-e and-f). Associated normals to the new points are simply set as the corresponding normals of each clipping plane.

Finally, in order to obtain the reconstructed geometry of the foam from the set of suitable points and normals, a Poisson surface reconstruction is performed⁶⁷ using the eponymous CGAL package https://doc.cgal.org/latest/Poisson_surface_reconstruction_3. At each point the Poisson surface reconstruction method requires an associated normal. For a given point its normal is obtained as the local normal of its associated ellipsoid at that point position. Figure 18 shows the set of suitable points extracted from the data described in Section 3.1, using an azimuthal angle increment $\Delta\theta = 10^\circ$. The Poisson surface reconstruction algorithm provided in the CGAL package can be tuned via three parameters (see Table 3). These three parameters, denoted α , T_s and, S_a control the quality and refinement of the mesh which is obtained from the discretised ellipsoids. They are directly related to the parameters of the CGAL function *poisson_surface_reconstruction_delaunay*.

Ultimately, a B-REP of the surface geometry is then obtained as a "geo" file describing vertices positions, edges and faces relations that can be used by the GMSH software⁶⁸. The advantage of having a meshable B-REP is that the 3D generated mesh can be, to some extent, "tuned" for satisfying some precise needs. For instance, the 3D generated mesh can be locally refined where needed. Moreover, the GMSH software easily allows associating several geometries together via boolean operations. For instance, one may consider to unite the surface geometry with a rectangular plate and conduct some thermal simulations with a dedicated solver. Figure 19 shows an extracted mesh compared to the threshold CT-scan images. It can be seen that the 3D mesh closely reproduces the different morphological characteristics of the foam, although the obtained porosity of 90.2% is quite different from the experimental 93% porosity. For the Ellipsoidal Model this difference, as suggested by the Hausdorff distance in Figure 19, is due to the fact that the ellipsoidal model seems to accumulate more matter than needed where struts meet. This problem could probably be alleviated by discretising the circumscribing auxiliary polyhedra instead of their associated auxiliary ellipsoids. Indeed, as each polyhedron contains its corresponding ellipsoid, the obtained porosity can only increase and sharp features should be better reconstructed. However, in any case, it should be noted that, despite the fact that the DN-CT-SCAN

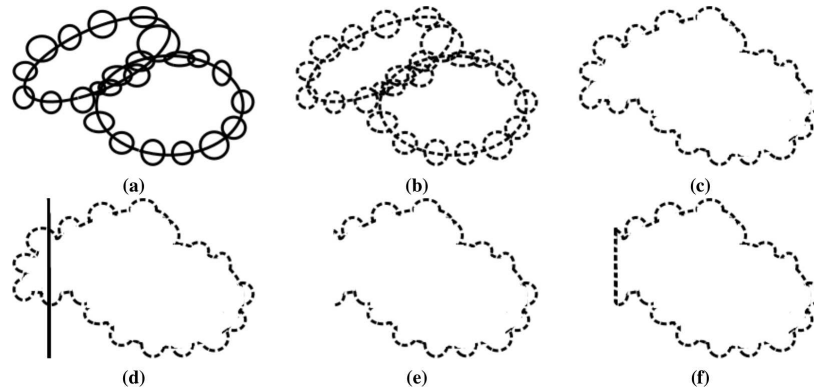


FIGURE 17 Schematics of the reconstruction of the geometry from the ellipsoids obtained in Section 2.2. (a) Obtained ellipsoids from Section 2.2. (b) Discretised ellipsoids. (c) Only points strictly not inside ellipsoids are kept. (d) Application of clipping planes for discarding points too close from boundaries. (e) Set of points with “holes”. (f) “Holes” filled.

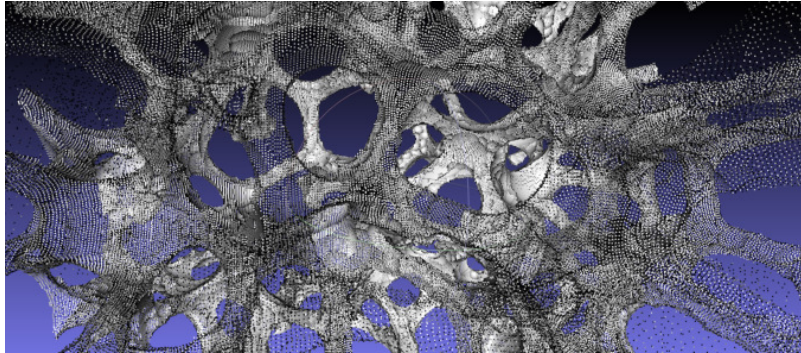


FIGURE 18 View inside the set of points extracted from the data described in Section 3.1.

TABLE 3 Parameters used in the geometric reconstruction of the CT-scan data presented in Section 3.1 for the Ellipsoidal Model.

Parameter	Value	Description
α	30°	Minimum triangle angle.
T_s	600.0	Maximum triangle size w.r.t. point set average spacing.
S_a	0.75	Surface approximation error w.r.t. point set average spacing.
ISO_{param}	1.0	Iso-surface parameter on which lie the extracted points.
$\Delta\theta$	10°	Azimuthal angle increment for discretising ellipsoids.

model using polyhedral packing presents a better porosity value than the Ellipsoidal model, both models present very similar structures and Hausdorff distances as it can be observed in Figures 16-b and 19.

It is worth noting that the *Ellipsoidal Model* is also able to reconstruct local features of the microstructure such as the typical tendency of struts to be thicker near their vertices than at their centre¹⁶. But this has also the capability to reproduce small defects as illustrated in Figure 20 without the need of some dedicated parametrisation.

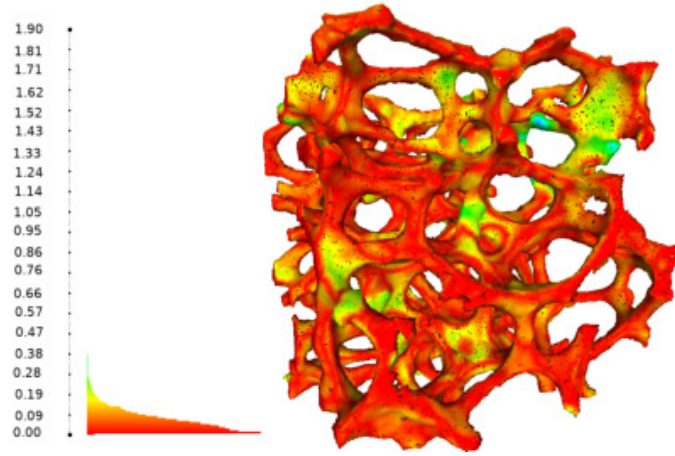


FIGURE 19 Visual representation of the Hausdorff distance in mm between the CT-scan image and the meshes extracted using Ellipsoidal Model.

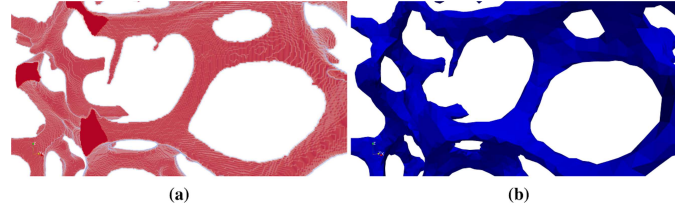


FIGURE 20 (a) Presence of a defect (spike) visible on the upper left-hand side of a 3D CT-scan image of a strut. (b) Reproduction of this defect by the *Ellipsoidal Model*.

3.1.5 | Summarising algorithm

In order to give a global insight of the whole reconstruction process, algorithm 1 briefly summarises all the preceding steps from the raw 3D-CT image to the final surface geometry.

Algorithm 1 Ellipsoidal Model summarising algorithm

Input: 3D CT-scan image I of a foam.

Output: Surface geometry G of the foam.

1. $I_T \leftarrow \text{threshold}(I)$
 2. $I_D \leftarrow \text{distance transform}(I_T)$
 3. $I_{Dopt} \leftarrow \text{distance processing}(I_D)$, optional
 4. $I_{max} \leftarrow \text{local maxima from } I_{D(opt)}$
 5. $E_{parent} \leftarrow \text{parent ellipsoids seeded from } I_{max} \text{ and with obstacles from } I_T$.
 6. $E_{aux} \leftarrow \text{auxiliary ellipsoids seeded from } E_{parents} \text{ and with obstacles from } I_T \text{ and artificial obstacles } E_{parents}$.
 7. $\{P, \vec{N}\} \leftarrow \text{points and associated normals from discretisations of } E_{parent} \text{ and } E_{aux} \text{ which do not lie strictly inside any ellipsoid.}$
 8. $\{P, \vec{N}\} \leftarrow \text{update with points and normals on boundaries}$
 9. $G \leftarrow \text{Poisson surface reconstruction using } \{P, \vec{N}\}$
-

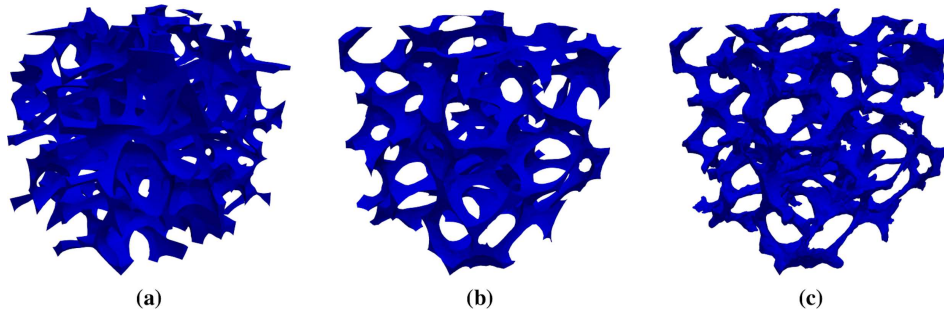


FIGURE 21 Meshed RVEs used for the simulations and generated from: (a) DN-CT-SCAN model using ellipsoids, (b) DN-CT-SCAN model using polyhedra, (c) Ellipsoidal Model. Around ~ 100.000 nodes and ~ 70.000 tetrahedral elements were used.

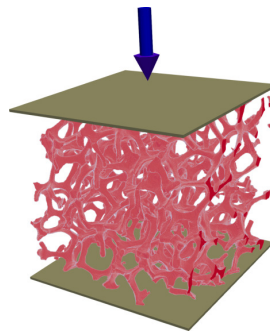


FIGURE 22 Experimental setup for the uniaxial compression test: top and bottom extremities molded into a small casting to ensure a stiff and stable fixture. Sides were left free.

4 | FEM SIMULATIONS: UNIAXIAL COMPRESSION TEST ON OPEN FOAM SAMPLE

In order to demonstrate the ability of the CT scan-based RVE generation to reproduce the structural properties of open foams by both the DN-CT-SCAN and the Ellipsoidal Model, finite element simulations have been conducted using the generated meshes obtained from the industrial aluminium open foam sample presented in section 3.1. More precisely, three meshes have been considered: two using the DN-CT-SCAN model, respectively obtained from the parent ellipsoids and associated polyhedra (Figure 21-a and-b), and one using the Ellipsoidal Model (Figure 21-c). In all cases, the considered RVEs have sizes of approximately $10 \times 10 \times 10 \text{ mm}^3$ and contain around 25 pores.

Simulations using these three RVEs were conducted using the finite element procedures proposed in^{91,92} and have been qualitatively compared against experimental measurements of an uniaxial compression reported in⁶⁶.

4.1 | Experimental data

The mechanical behaviour of the cubic sample of aluminium foam described in Section 3.1 were investigated by uniaxial compression tests using an ElectroPulsTM E10000 universal testing machine of Instron Ltd., Pfungstadt, Germany. A displacement control using a quasi-static strain rate of $5 \cdot 10^{-3} \text{ s}^{-1}$ was applied for each test. The top and bottom extremities of the studied sample were molded into a small casting to generate plane parallel plates as force transmission points for the compression tests (see Figure 22). The Wood's alloy guarantees a gentle molding and demolding, providing a stiff and stable fixture at the same time. These requirements cannot be adequately met by polymer resins. The boundaries orthogonal to the compression directions were left free.

TABLE 4 Averaged struts material properties identified for the isotropic hardening law used for the simulations.

Material property	Value (MPa)	Description
E	3968.12	Young's modulus.
σ^0	46.35	Initial yield stress.
H_{iso}	214.61	Linear hardening.

4.2 | Material properties

Simulations were carried out using for the struts a linear hardening hyperelastic-based J_2 -elasto-plastic material law applied for large strains (see Appendix A in Nguyen et al.⁹¹ for details), with the isotropic hardening law given in equation 8.

$$\sigma_y^0(\bar{\epsilon}^{pl}) = \sigma_0 + H_{iso}\bar{\epsilon}^{pl} \quad (8)$$

Where $\bar{\epsilon}^{pl}$ is the equivalent plastic strain.

Struts material properties required to parametrise the material law were identified in⁶⁶, using an inverse identification procedure based on compression tests of single pores. As the provided values tends to vary from one pore to another, averaged material properties have been considered. Table 4 reports the material properties used for the simulations.

4.3 | Boundary conditions

In order to understand the numerical response of the RVEs, several boundary conditions were tested. This was required by the fact that the three RVEs extracted from the CT-scan data are rather small compared to the samples on which experimental measurements were conducted. Namely, for each RVE, three sets of boundary conditions were considered (see Figure 23): enforcement of free boundary conditions which are a simple uniaxial compression, mixed boundary conditions which are obtained by imposing an uniaxial load while constraining struts extremities to lie in common planes, and periodic boundary conditions using a 5th-order Lagrangian polynomial based interpolation⁹³.

More precisely, struts nodes in contact with the top plane were constrained to vertically follow its displacement, while they were free to move in the horizontal directions. Similarly, struts nodes in contact with the bottom plane were vertically constrained by it, while free to move in the horizontal directions. However, in order to avoid rigid body motion, two nodes in contact with the bottom plane were constrained as follows. The first one had also its x and y coordinates fixed, while the second one has its x coordinate fixed.

The free boundary conditions had no other imposed conditions, and struts extremities not in contact with the planes were free to move. For the mixed boundary conditions, struts extremities located on a given lateral side were constrained to move within the same vertical plane.

Finally, for the periodic boundary conditions, displacements of struts extremities from one lateral side were constrained in terms of the displacement of the struts extremities located on the corresponding opposite side following an interpolation method as described in⁹² to constrain periodic boundary conditions for non-periodic meshes. For these different kinds of boundary conditions, uniaxial tension can be obtained by selecting the components of the macroscopic scale deformation gradient which are enforced during the constrained resolution of the RVE, see details in Section 3.5 of paper⁹⁴.

4.4 | Comparison of simulations against experimental data

4.4.1 | Periodic boundary conditions

Simulations of uniaxial compression were conducted on the three considered RVEs showed in Figure 21 using periodic boundary conditions with a 5th-order Lagrangian polynomial based interpolation⁹³. Figures 24(a,b) report on the red curves the (relative) strain-stress curves obtained from the simulations for each RVE along the compression direction. From this figure, some over-stiffness can be observed with respect to the experimental data in the obtained curves. As shown in⁹³, the obtained strain-stress curves using Lagrangian polynomial enforced periodic boundary conditions show a convergence behaviour with higher degrees

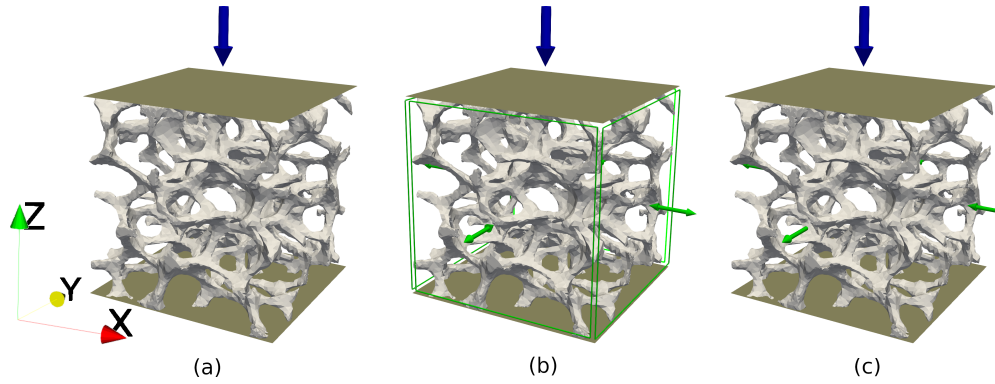


FIGURE 23 Tested boundary conditions for a simple uniaxial compression: (a) free boundary conditions, (b) mixed boundary conditions (uniaxial load while ensuring struts extremities lie in common planes), (c) periodic boundary conditions using Lagrangian polynomial interpolation⁹³.

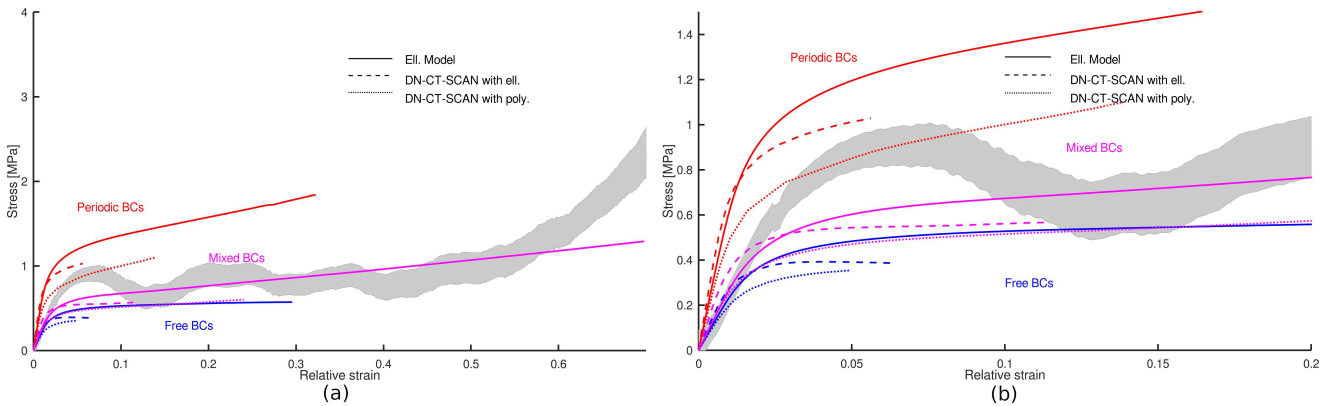


FIGURE 24 (a) Simulations of a uniaxial compression test on an open cubic sample of aluminium foam (see Section 3.1) with periodic boundary conditions (red curves), free boundary conditions (blue curves) and mixed boundary conditions (magenta curves); using ≈ 70.000 tetrahedra in all the cases. Obtained (relative) strain-stress curves using the three generated RVEs presented in Figure 21, against experimental measurements (grey area). (b) Zoom of Figure (a).

of interpolation. In order to investigate if the origin of the observed over-stiffness is due to the use of a too small interpolation degree, a convergence study of the strain-stress curves with respect to the interpolation degree was conducted. From this study it has been observed that the choice of the interpolation degree cannot explain the observed discrepancies between the simulations and the experimental data. Especially, the obtained initial slopes in the linear deformation regime are very similar for all the tested interpolation degrees and does not comply with the experimental measurements. Therefore, it has been concluded that the enforcement of periodic boundary conditions adds extra constraints on the deformation of the struts and cannot be realistic for the considered RVEs because of their reduced sizes and the non-periodicity of their geometry.

4.4.2 | Free boundary conditions

As the enforcement of periodic boundary conditions discussed in section 4.4.1 leads to an over-stiffness behaviour, one can release them and just consider the three RVEs with free lateral boundaries. Figures 24(a,b) report on the blue curves the obtained strain-stress curves for the three considered RVEs when imposing a simple uniaxial compression. It can be observed that, for this case, the result presents some over-softness with respect to experimental data. Though the initial slopes in the linear deformation regime for all three considered RVEs are within the experimental scattering, the free boundary conditions induce unrealistic deformations as compared to the other boundary conditions and to what can be expected in an embedded body (Figure 25).

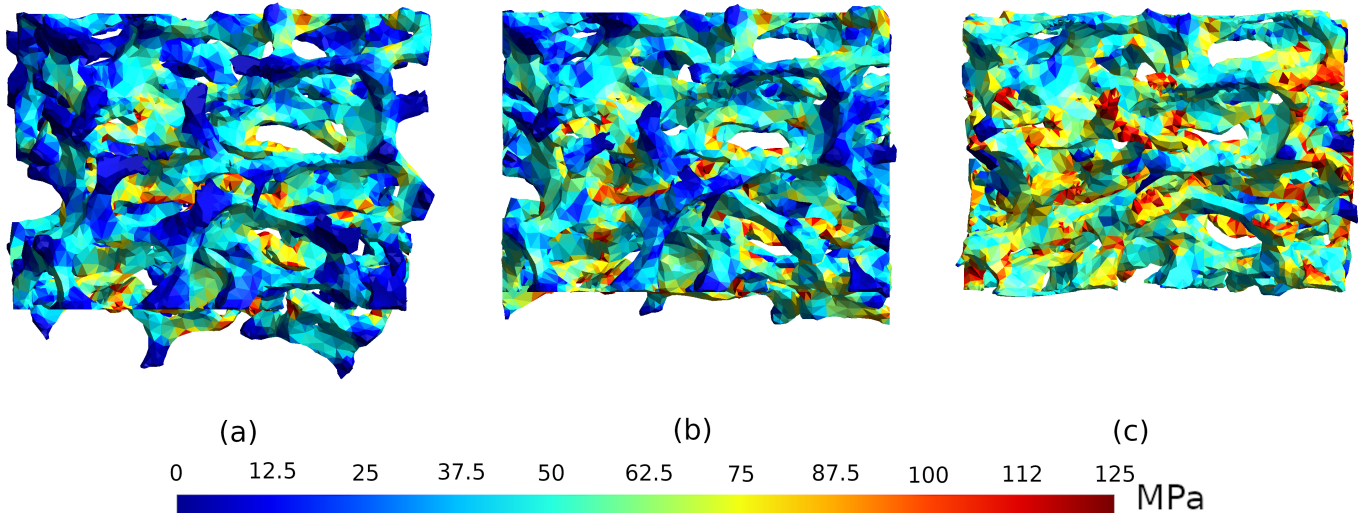


FIGURE 25 Simulations of uniaxial compression tests on an open cubic aluminium foam (see Section 3.1) using the RVE generated by the Ellipsoidal Model for different boundary conditions. (a) Free, (b) mixed and (c) periodic. The von Mises stresses are plotted on the 30 % deformed RVE.

4.4.3 | Mixed boundary conditions

From the previous sections 4.4.1 and 4.4.2, the periodic and free boundary conditions induce, respectively, over-stiffness and over-softness in the simulated behaviour of all three considered RVEs. Figure 24-b reports on the magenta curves the strain-stress curves obtained with the considered RVEs. It can be seen that the mixed boundary conditions avoid imposing artificial constraints on the struts and that the computed strain-stress curves exhibit a comparable behaviour as observed experimentally.

Indeed, the initial slope in the linear deformation regime is rather well reproduced for the polyhedra-based DN-CT-SCAN model and the Ellipsoidal Model (which present very similar geometrical features, contrary to the quite different ellipsoid-based DN-CT-SCAN model), though they display plastic deformation quite early compared to the experimental results. Moreover, as can be seen in Figure 24-a, the plateau regime is rather well reproduced by polyhedra-based DN-CT-SCAN model and the Ellipsoidal Model (magenta curves). At high relative strains, around 60 % and beyond, struts begins to pile-up against each other and a so-called densification regime is experimentally observed as a fast stress increase occurs for small deformation increments. Here, the densification regime was not reproduced by the FEM model as this one allowed the struts to interpenetrate, thus preventing any struts stacking.

It should be noted that the RVEs generated by the DN-CT-SCAN model did in general not allow to compute deformations beyond 30 %, since the presence of narrow and/or high curvature regions cause the presence of bad-shaped mesh elements, which, in turn, prevented the FEM simulations to continue due to these elements exhibiting negative Jacobians when deformed. A solution to this issue was proposed in⁸⁸ by optimising meshes using the Persson-Strang analogy, and might be considered in the future for improving the meshing of the DN-CT-SCAN model.

4.4.4 | Discussion: numerical convergence

Strain-stress simulations results presented in Figure 24 were produced using order-2 tetrahedral meshes containing approximately 70.000 tetrahedra. In order to ensure that convergence was indeed obtained, additional simulations with an increasing number of tetrahedra were conducted.

As the Ellipsoidal Model is able to provide a surface geometry, it was easy to extract several meshes with an increasing number of tetrahedra from it by using the Gmsh⁶⁸ software. Figure 26 shows the obtained strain-stress curves for four different meshes containing 42.740 up to 430.001 tetrahedra. It can be observed from Figure 26 and Table 5 that the differences between the strain-stress curves from the mesh using 70.704 tetrahedra to the finest mesh and for all three boundary conditions can be considered low (i.e. under 10% relative difference at a relative strain of 20%).

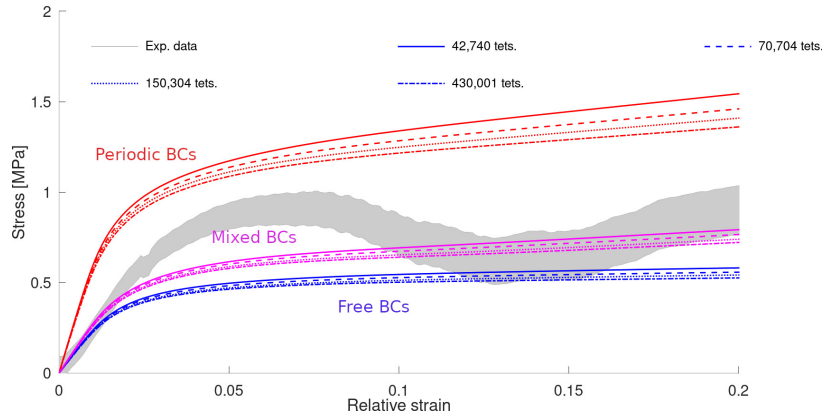


FIGURE 26 Simulations of a uniaxial compression test on an open cubic sample of aluminium foam (see Section 3.1), using the geometry provided by the Ellipsoidal Model, with the three considered boundary conditions, using order-2 meshes with different numbers of tetrahedra.

TABLE 5 Relative differences between the computed strain-stress curves obtained at a relative strain of 20% using different meshes computed from the geometry provided from the Ellipsoidal Model. The differences were computed using a reference mesh consisting in 430.001 tetrahedra.

Boundary conditions	42.740 tets.	70.704 tets.	150.304 tets.
Free	11.43%	5.45%	3.3%
Mixed	10.4%	6.5%	2.9%
Periodic	13.0%	7.8%	4.1%

5 | CONCLUSION AND PERSPECTIVES

In this contribution two models for the reconstruction of the geometry of foams from 3D CT-scan images were presented: the *DN-CT-SCAN* model and the *Ellipsoidal Model*.

Both models rely on a first step consisting into an image analysis of 3D CT-scan images. The image analysis stage provides the models with uniquely fitted ellipsoids and associated polyhedra to identified cells. This image analysis step avoids using computationally expensive algorithm such as the watershed and the H-maxima transform. Instead, it relies on the detection of local maxima of the distance transform of the images, and then on the individual constrained growth and clustering of ellipsoids. This procedure allows processing slice by slice (a.k.a. streaming) huge 3D CT-scan images which cannot be loaded into the available RAM (with the limitation that the minimum slice thickness is governed by the maximum cell size into that slice). Alternatively, it is also possible to parallelise the image analysis among multiple cores each with a limited amount of available memory. The effectiveness of this streaming process has been demonstrated in section 2.4 for both artificial and real-world 3D CT-scan images of foams. Furthermore, this image analysis step can be used by other reconstruction models by providing them cell identifications as points, ellipsoids and/or associated polyhedra.

Regarding the accuracy of the reconstruction by both models, section 3 has shown that they can faithfully reproduce the microstructure of the considered foam. Besides, the *Ellipsoidal model* is also able to reproduce any local feature visible in the 3D CT-scan images without the need of any additional parametrisation or additional optimisation procedure. Eventually, this model provides a boundary representation (B-REP) which offers more flexibility than 3D meshes for FEM models. For instance for adding some external geometries using boolean operations for the aim of satisfying any specific needs or study.

Concerning the use of the reconstructed geometries by both models inside FEM simulations, section 4 illustrates that the geometries can indeed be successfully used in such simulations for assessing the mechanical behaviour of foams; with a good qualitative agreement with respect to experimental data.

About possible improvements, the streaming part of the image analysis step can be further improved by considering blocks instead of slices in 3D CT-scan images. The *Ellipsoidal Model* currently uses the discretised auxiliary ellipsoids and a standard Poisson surface reconstruction algorithm for reconstruction the geometry. Improvements on both counts can be performed by using the discretised associated auxiliary polyhedra to the auxiliary ellipsoids for the first, and some more advanced Poisson surface reconstructions taking into account sharp edges for the second as proposed in⁹⁵.

ACKNOWLEDGMENTS

The research has been funded by the *Actions de recherche concertées ARC 09/14-02 BRIDGING – From imaging to geometrical modeling of complex micro-structured materials: Bridging computational engineering and material science* from the *Direction générale de l'Enseignement non obligatoire de la Recherche scientifique, Direction de la Recherche scientifique, Communauté française de Belgique*, and granted by the *Académie Universitaire Wallonie-Europe* and by the “F.R.S.F. N.R.S. EnlightenIt project”, grant number PDR T.0038.16.

Computational resources have been provided by the supercomputing facilities of the *Consortium des Équipements de Calcul Intensif en Fédération Wallonie Bruxelles (CECI)* funded by the *Fond de la Recherche Scientifique de Belgique (FRS-FNRS)*.

References

1. Gibson LJ, Ashby MF. *Cellular Solids: Structure and Properties*. Cambridge: Cambridge University Press. second ed. 1997
2. Lautensack C. Fitting three-dimensional Laguerre tessellations to foam structures. *Journal of Applied Statistics* 2008; 35(9): 985–995. doi: 10.1080/02664760802188112
3. Jung A, Beex LA, Diebels S, Bordas SP. Open-cell aluminium foams with graded coatings as passively controllable energy absorbers. *Materials and Design* 2015; 87: 36–41. doi: 10.1016/j.matdes.2015.07.165
4. Yin S, Rayess N. Characterization of Polymer-metal Foam Hybrids for Use in Vibration Dampening and Isolation. *Procedia Materials Science* 2014; 4: 311–316. doi: 10.1016/j.mspro.2014.07.564
5. Villafán-Vidales H, Abanades S, Caliot C, Romero-Paredes H. Heat Transfer Simulation in a Thermochemical Solar Reactor Based on a Volumetric Porous Receiver. *Applied Thermal Engineering* 2011; 31(16): 3377-3386. doi: 10.1016/j.applthermaleng.2011.06.022
6. Destefanis R, Schäfer F, Lambert M, Faraud M. Selecting Enhanced Space Debris Shields for Manned Spacecraft. *International Journal of Impact Engineering* 2006; 33(1-12): 219-230. doi: 10.1016/j.ijimpeng.2006.09.065
7. Banhart J. Manufacture, characterisation and application of cellular metals and metal foams. *Progress in Materials Science* 2001; 46(6): 559–632. doi: 10.1016/S0079-6425(00)00002-5
8. Singh S, Bhatnagar N. A survey of fabrication and application of metallic foams (1925-2017). *Journal of Porous Materials* 2018; 25(2): 537–554. doi: 10.1007/s10934-017-0467-1
9. Plateau JAF. *Statique expérimentale et théorique des liquides soumis aux seules forces moléculaires*. Gauthier-Villars . 1873.
10. Kraynik AM, Reinelt DA, van Swol F. Structure of Random Monodisperse Foam. *Physical Review E* 2003; 67(3). doi: 10.1103/PhysRevE.67.031403
11. Spetl A, Brereton T, Duan Q, et al. Fitting Laguerre tessellation approximations to tomographic image data. *Philosophical Magazine* 2016; 96(2): 166–189. doi: 10.1080/14786435.2015.1125540
12. Godehardt M, Schladitz K. *Geometric Characterisation of Light Weight Composites Using Computer Tomographic Images* . ECNDT 2006 - We.1.6.3, 2006.

13. Youssef S, Maire E, Gaertner R. Finite element modelling of the actual structure of cellular materials determined by X-ray tomography. *Acta Materialia* 2005; 53(3): 719–730. doi: 10.1016/j.actamat.2004.10.024
14. Zhu X, Ai S, Fang D, Liu B, Lu X. A novel modeling approach of aluminum foam based on MATLAB image processing. *Computational Materials Science* 2014; 82: 451–456. doi: 10.1016/j.commatsci.2013.10.020
15. Natesaiyer K, Chan C, Sinha-Ray S, et al. X-ray CT imaging and finite element computations of the elastic properties of a rigid organic foam compared to experimental measurements: insights into foam variability. *Journal of Materials Science* 2015; 50(11): 4012–4024. doi: 10.1007/s10853-015-8958-4
16. Redenbach C. Modelling foam structures using random tessellations. In: Milan: ESCULAPIO Pub. Co. 2009.
17. Kampf J, Schlachter AL, Redenbach C, Liebscher A. Segmentation, statistical analysis, and modelling of the wall system in ceramic foams. *Materials Characterization* 2015; 99: 38–46. doi: 10.1016/j.matchar.2014.11.008
18. Vincent L. Morphological grayscale reconstruction in image analysis: applications and efficient algorithms. *IEEE Transactions on Image Processing* 1993; 2(2): 176–201. doi: 10.1109/83.217222
19. Soille P. *Morphological Image Analysis*. 24. Berlin, Heidelberg: Springer Berlin Heidelberg . 1999
20. Sun H, Yang J, Ren M. A fast watershed algorithm based on chain code and its application in image segmentation. *Pattern Recognition Letters* 2005; 26(9): 1266–1274. doi: 10.1016/j.patrec.2004.11.007
21. Bieniek A, Burkhardt H, Freiburg A, Marschner H, Schreiber G, Nolle M. A parallel watershed algorithm. In: Proceedings of the 10th Scandinavian Conference on Image Analysis (SCIA'97), 1997 (pp. 237–244).
22. Körbes A, Lotufo R, Vitor GBG, Ferreira JVJ. A Proposal for a Parallel Watershed Transform Algorithm for Real-Time Segmentation. In: Proceedings of Workshop de Visao Computacional WVC, 2009.
23. Al-Raoush R, Alshibli KA. Distribution of local void ratio in porous media systems from 3D X-ray microtomography images. *Physica A: Statistical Mechanics and its Applications* 2006; 361(2): 441–456. doi: 10.1016/j.physa.2005.05.043
24. Veyhl C, Belova I, Murch G, Fiedler T. Finite Element Analysis of the Mechanical Properties of Cellular Aluminium Based on Micro-Computed Tomography. *Materials Science and Engineering: A* 2011; 528(13-14): 4550-4555. doi: 10.1016/j.msea.2011.02.031
25. Fiedler T, Solórzano E, Garcia-Moreno F, Öchsner A, Belova I, Murch G. Computed Tomography Based Finite Element Analysis of the Thermal Properties of Cellular Aluminium. *Materialwissenschaft und Werkstofftechnik* 2009; 40(3): 139-143. doi: 10.1002/mawe.200900419
26. Montminy MD, Tannenbaum AR, Macosko CW. The 3D structure of real polymer foams. *Journal of Colloid and Interface Science* 2004; 280(1): 202–211. doi: 10.1016/j.jcis.2004.07.032
27. Legrain G, Cartraud P, Perreard I, Moës N. An X-FEM and level set computational approach for image-based modelling: Application to homogenization. *International Journal for Numerical Methods in Engineering* 2011; 86(7): 915–934. doi: 10.1002/nme.3085
28. Thomson W. LXIII. On the Division of Space with Minimum Partitional Area. *The London, Edinburgh, and Dublin Philosophical Magazine and Journal of Science* 1887; 24(151): 503–514.
29. Weaire D, Phelan R. A Counter-Example to Kelvin's Conjecture on Minimal Surfaces. *Philosophical Magazine Letters* 1994; 69(2): 107-110. doi: 10.1080/09500839408241577
30. Hardenacke V, Hohe J. Assessment of space division strategies for generation of adequate computational models for solid foams. *International Journal of Mechanical Sciences* 2010; 52(12): 1772–1782. doi: 10.1016/j.ijmecsci.2010.09.011
31. Bracconi M, Ambrosetti M, Maestri M, Groppi G, Tronconi E. A systematic procedure for the virtual reconstruction of open-cell foams. *Chemical Engineering Journal* 2017; 315: 608–620. doi: 10.1016/j.cej.2017.01.069

32. Zhu W, Blal N, Cunsolo S, Baillis D. Effective elastic properties of periodic irregular open-cell foams. *International Journal of Solids and Structures* 2018; 143: 155–166. doi: 10.1016/j.ijsolstr.2018.03.003
33. Wan F, Tran MP, Leblanc C, et al. Experimental and Computational Micro-Mechanical Investigations of Compressive Properties of Polypropylene/Multi-Walled Carbon Nanotubes Nanocomposite Foams. *Mechanics of Materials* 2015; 91: 95–118. doi: 10.1016/j.mechmat.2015.07.004
34. Van Der Burg MWD, Shulmeister V, Van Der Geissen E, Marissen R. On the Linear Elastic Properties of Regular and Random Open-Cell Foam Models. *Journal of Cellular Plastics* 1997; 33(1): 31–54. doi: 10.1177/0021955X9703300103
35. Lautensack C, Sych T. 3D Image Analysis of Open Foams Using Random Tessellations. *Image Analysis & Stereology* 2006; 25(2): 87–93. doi: 10.5566/ias.v25.p87-93
36. Liebscher A, Proppe C, Redenbach C, Schwarzer D. Stochastic multiscale modeling of metal foams. *Procedia IUTAM* 2013; 6: 87–96. doi: 10.1016/j.piutam.2013.01.010
37. Redenbach C. Microstructure Models for Cellular Materials. *Computational Materials Science* 2009; 44(4): 1397–1407. doi: 10.1016/j.commatsci.2008.09.018
38. Redenbach C, Shklyar I, Andrä H. Laguerre tessellations for elastic stiffness simulations of closed foams with strongly varying cell sizes. *International Journal of Engineering Science* 2012; 50(1): 70–78. doi: 10.1016/j.ijengsci.2011.09.002
39. Vecchio I, Redenbach C, Schladitz K. Angles in Laguerre tessellation models for solid foams. *Computational Materials Science* 2014; 83: 171–184. doi: 10.1016/j.commatsci.2013.11.017
40. Liebscher A. Laguerre approximation of random foams. *Philosophical Magazine* 2015; 95(25): 2777–2792. doi: 10.1080/14786435.2015.1078511
41. Marvi-Mashhadi M, Lopes C, LLorca J. Modelling of the mechanical behavior of polyurethane foams by means of micromechanical characterization and computational homogenization. *International Journal of Solids and Structures* 2018; 146: 154–166. doi: 10.1016/j.ijsolstr.2018.03.026
42. Marvi-Mashhadi M, Lopes C, LLorca J. High fidelity simulation of the mechanical behavior of closed-cell polyurethane foams. *Journal of the Mechanics and Physics of Solids* 2020; 135: 103814. doi: 10.1016/j.jmps.2019.103814
43. Lautensack C, Zuyev S. Random Laguerre tessellations. *Advances in Applied Probability* 2008; 40(3): 630–650. doi: 10.1239/aap/1222868179
44. Boissonnat JD, Teillaud M. *Effective Computational Geometry for Curves and Surfaces*. Springer Berlin Heidelberg . 2006
45. Schaller FM, Kapfer SC, Evans ME, et al. Set Voronoi diagrams of 3D assemblies of aspherical particles. *Philosophical Magazine* 2013; 93(31–33): 3993–4017. doi: 10.1080/14786435.2013.834389
46. Alpers A, Brieden A, Gritzmann P, Lyckegaard A, Poulsen HF. Generalized balanced power diagrams for 3D representations of polycrystals. *Philosophical Magazine* 2015; 95(9): 1016–1028. doi: 10.1080/14786435.2015.1015469
47. Šedivý O, Brereton T, Westhoff D, et al. 3D reconstruction of grains in polycrystalline materials using a tessellation model with curved grain boundaries. *Philosophical Magazine* 2016; 96(18): 1926–1949. doi: 10.1080/14786435.2016.1183829
48. Šedivý O, Dake JM, Krill CE, Schmidt V, Jäger A. Description of the 3D morphology of grain boundaries in aluminum alloys using tessellation models generated by ellipsoids. *Image Analysis and Stereology* 2017; 36(1): 5–13. doi: 10.5566/ias.1656
49. Bourne DP, Kok PJJ, Roper SM, Spanjer WDT. Laguerre tessellations and polycrystalline microstructures: a fast algorithm for generating grains of given volumes. *Philosophical Magazine* 2020; 100(21): 2677–2707. doi: 10.1080/14786435.2020.1790053
50. Bezrukov A, BargielM, Stoyan D. Statistical Analysis of Simulated Random Packings of Spheres. *Part. Part. Syst. Charact.* 2002; 19(2): 111–118. doi: 10.1002/1521-4117(200205)19:2<111::AID-PPSC111>3.0.CO;2-M

51. Bezrukov A, Stoyan D, Bargiel M. Spatial Statistics for Simulated Packings of Spheres. *Image Analysis & Stereology* 2001; 20(3): 203. doi: 10.5566/ias.v20.p203-206
52. Kraynik AM, Reinelt D, van Swol F. Structure of Random Foam. *Physical Review Letters* 2004; 93(20). doi: 10.1103/PhysRevLett.93.208301
53. Kraynik AM. The Structure of Random Foam. *Adv. Eng. Mater.* 2006; 8(9): 900-906. doi: 10.1002/adem.200600167
54. Vecchio I, Redenbach C, Schladitz K, Kraynik AM. Improved Models of Solid Foams Based on Soap Froth. *Computational Materials Science* 2016; 120: 60-69. doi: 10.1016/j.commatsci.2016.03.029
55. Moorthy S, Ghosh S. A model for analysis of arbitrary composite and porous microstructures with voronoi cell finite elements. *International Journal for Numerical Methods in Engineering* 1996; 39(14): 2363–2398. doi: 10.1002/(SICI)1097-0207(19960730)39:14<2363::AID-NME958>3.0.CO;2-D
56. Redenbach C. Microstructure models for cellular materials. *Computational Materials Science* 2009; 44(4): 1397–1407. doi: 10.1016/j.commatsci.2008.09.018
57. Wu Y, Zhou W, Wang B, Yang F. Modeling and characterization of two-phase composites by Voronoi diagram in the Laguerre geometry based on random close packing of spheres. *Computational Materials Science* 2010; 47(4): 951–961. doi: 10.1016/j.commatsci.2009.11.028
58. Roberts A, Garboczi E. Elastic properties of model random three-dimensional open-cell solids. *Journal of the Mechanics and Physics of Solids* 2002; 50(1): 33–55. doi: 10.1016/S0022-5096(01)00056-4
59. Jang WY, Kraynik AM, Kyriakides S. On the Microstructure of Open-Cell Foams and Its Effect on Elastic Properties. *International Journal of Solids and Structures* 2008; 45(7): 1845-1875. doi: 10.1016/j.ijsolstr.2007.10.008
60. Sonon B, François B, Massart TJ. An advanced approach for the generation of complex cellular material representative volume elements using distance fields and level sets. *Computational Mechanics* 2015; 56(2): 221–242. doi: 10.1007/s00466-015-1168-8
61. Kilingar N, Ehab Moustafa Kamel K, Sonon B, Massart TJ, Noels L. Computational generation of open-foam representative volume elements with morphological control using distance fields. *European Journal of Mechanics - A/Solids* 2019; 78: 103847. doi: 10.1016/j.euromechsol.2019.103847
62. Barnes AT, Ravi-Chandar K, Kyriakides S, Gaitanaros S. Dynamic crushing of aluminum foams: Part i - Experiments. *International Journal of Solids and Structures* 2014; 51(9): 1631–1645. doi: 10.1016/j.ijsolstr.2013.11.019
63. Gaitanaros S, Kyriakides S. Dynamic crushing of aluminum foams: Part II – Analysis. *International Journal of Solids and Structures* 2014; 51(9): 1646–1661. doi: 10.1016/j.ijsolstr.2013.11.020
64. Gong L, Kyriakides S. Compressive Response of Open Cell Foams Part II: Initiation and Evolution of Crushing. *International Journal of Solids and Structures* 2005; 42(5-6): 1381-1399. doi: 10.1016/j.ijsolstr.2004.07.024
65. Jung A, Diebels S. Microstructural Characterisation and Experimental Determination of a Multiaxial Yield Surface for Open-Cell Aluminium Foams. *Materials & Design* 2017; 131: 252-264. doi: 10.1016/j.matdes.2017.06.017
66. Heinze S, Bleistein T, Düster A, Diebels S, Jung A. Experimental and Numerical Investigation of Single Pores for Identification of Effective Metal Foams Properties: Experimental and Numerical Investigation of Single Pores for Identification of Effective Metal Foams Properties. *ZAMM - Journal of Applied Mathematics and Mechanics / Zeitschrift für Angewandte Mathematik und Mechanik* 2018; 98(5): 682-695. doi: 10.1002/zamm.201700045
67. Kazhdan M, Bolitho M, Hoppe H. Poisson Surface Reconstruction. *Eurographics Symposium on Geometry Processing* 2006: 61–70.
68. Geuzaine C, Remacle JF. Gmsh: A 3-D finite element mesh generator with built-in pre- and post-processing facilities. *International Journal for Numerical Methods in Engineering* 2009; 79(11): 1309–1331. doi: 10.1002/nme.2579

69. Schroeder W. *The ITK Software Guide Second Edition Updated for ITK version 2 . 4*. 525. Kitware, Inc. second ed. 2005
70. Zuluaga MA, Ibañez L, Peyrin F. Large Image Streaming using ITKv4. *The Insight Journal* 2011; January-Ju: 1–9.
71. Ohser J, Schladitz K. *Image processing and analysis*. Oxford: Clarendon Press . 2006.
72. Cheng J, Rajapakse JC. Segmentation of clustered nuclei with shape markers and marking function. *IEEE Transactions on Biomedical Engineering* 2009; 56(3): 741–748. doi: 10.1109/TBME.2008.2008635
73. Ridler, T.W. Calvard S. Picture Thresholding Using an Iterative Selection Method. *IEEE Transactions on Systems, Man and Cybernetics* 1978; 8(8): 630–632. doi: 10.1109/TSMC.1978.4310039
74. Sezgin M, Sankur B. Survey over image thresholding techniques and quantitative performance evaluation. *Journal of Electronic Imaging* 2004; 13(1): 146–165. doi: 10.1117/1.1631316
75. Maurer CR, Rensheng Qi , Raghavan V. A linear time algorithm for computing exact Euclidean distance transforms of binary images in arbitrary dimensions. *IEEE Transactions on Pattern Analysis and Machine Intelligence* 2003; 25(2): 265–270. doi: 10.1109/TPAMI.2003.1177156
76. Pham TQ. Non-maximum suppression using fewer than two comparisons per pixel. *Lecture Notes in Computer Science (including subseries Lecture Notes in Artificial Intelligence and Lecture Notes in Bioinformatics)* 2010; 6474 LNCS(PART 1): 438–451. doi: 10.1007/978-3-642-17688-3_41
77. Macia I. Generalized Computation of Gaussian Derivatives Using ITK. *The Insight Journal (December 2007)* 2007.
78. Deits R, Tedrake R. Computing Large Convex Regions of Obstacle-Free Space Through Semidefinite Programming. In: Akin HL, Amato NM, Isler V, Stappen v. dAF., eds. *Springer Tracts in Advanced Robotics*. 107 of *Springer Tracts in Advanced Robotics*. Springer International Publishing. 2015 (pp. 109–124)
79. Tita V, Caliri MF, Angélico RA, Canto RB. Experimental analyses of the poly(vinyl chloride) foams’ mechanical anisotropic behavior. *Polymer Engineering & Science* 2012; 52(12): 2654–2663. doi: 10.1002/pen.23222
80. Caliri Júnior MF, Soares GP, Angélico RA, Canto RB, Tita V. Study of an anisotropic polymeric cellular material under compression loading. *Materials Research* 2012; 15(3): 359–364. doi: 10.1590/S1516-14392012005000034
81. Andersons J, Kirpluks M, Stiebra L, Cabulis U. Anisotropy of the stiffness and strength of rigid low-density closed-cell polyisocyanurate foams. *Materials and Design* 2016; 92: 836–845. doi: 10.1016/j.matdes.2015.12.122
82. Mader K, Mokso R, Raufaste C, et al. Quantitative 3D characterization of cellular materials: Segmentation and morphology of foam. *Colloids and Surfaces A: Physicochemical and Engineering Aspects* 2012; 415: 230–238. doi: 10.1016/j.colsurfa.2012.09.007
83. Teferra K, Graham-Brady L. Tessellation growth models for polycrystalline microstructures. *Computational Materials Science* 2015; 102: 57–67. doi: 10.1016/j.commatsci.2015.02.006
84. Sander J, Ester M, Kriegel HP, Xu X. Density-based clustering in spatial databases: The algorithm GDBSCAN and its applications. *Data Mining and Knowledge Discovery* 1998; 2(2): 169–194. doi: 10.1023/A:1009745219419
85. Yildirim EA. On the Minimum Volume Covering Ellipsoid of Ellipsoids. *SIAM Journal on Optimization* 2006; 17(3): 621–641. doi: 10.1137/050622560
86. Nethercote N, Seward J. Valgrind. *ACM SIGPLAN Notices* 2007; 42(6): 89. doi: 10.1145/1273442.1250746
87. Wintiba B, Sonon B, Ehab Moustafa Kamel K, Massart TJ. An Automated Procedure for the Generation and Conformal Discretization of 3D Woven Composites RVEs. *Composite Structures* 2017; 180: 955-971. doi: 10.1016/j.compstruct.2017.08.010
88. Ehab Moustafa Kamel K, Sonon B, Massart TJ. An integrated approach for the conformal discretization of complex inclusion-based microstructures. *Computational Mechanics* 2019; 64(4): 1049–1071. doi: 10.1007/s00466-019-01693-4

89. Si H. TetGen, a Delaunay-Based Quality Tetrahedral Mesh Generator. *ACM Transactions on Mathematical Software* 2015; 41(2): 1-36. doi: 10.1145/2629697
90. Cignoni P, Rocchini C, Scopigno R. Metro: Measuring Error on Simplified Surfaces. *Computer Graphics Forum* 1998; 17(2): 167–174. doi: 10.1111/1467-8659.00236
91. Nguyen VD, Noels L. Computational homogenization of cellular materials. *International Journal of Solids and Structures* 2014; 51(11-12): 2183–2203. doi: 10.1016/j.ijsolstr.2014.02.029
92. Nguyen VD, Wu L, Noels L. Unified Treatment of Microscopic Boundary Conditions and Efficient Algorithms for Estimating Tangent Operators of the Homogenized Behavior in the Computational Homogenization Method. *Computational Mechanics* 2017; 59(3): 483-505. doi: 10.1007/s00466-016-1358-z
93. Nguyen VD, Bécchet E, Geuzaine C, Noels L. Imposing periodic boundary condition on arbitrary meshes by polynomial interpolation. *Computational Materials Science* 2012; 55: 390–406. doi: 10.1016/j.commatsci.2011.10.017
94. Nguyen VD, Wu L, Noels L. A micro-mechanical model of reinforced polymer failure with length scale effects and predictive capabilities. Validation on carbon fiber reinforced high-crosslinked RTM6 epoxy resin. *Mechanics of Materials* 2019; 133: 193-213. doi: 10.1016/j.mechmat.2019.02.017
95. Salman N, Yvinec M, Merigot Q. Feature preserving mesh generation from 3D point clouds. *Eurographics Symposium on Geometry Processing* 2010; 29(5): 1623–1632.

